Performance of Silicon Heterojunction Cells and Modules in Arctic Applications: Impact of Angle of Incidence, Air Mass, and Spectra on Energy Yield

By

Amanda Lewis

Thesis submitted to the University of Ottawa
in partial fulfillment of the requirements for the degree of
Master of Applied Science in Electrical Engineering and Computer Science

School of Electrical Engineering and Computer Science
Faculty of Engineering
University of Ottawa

Abstract

In Canada, many remote communities rely on diesel power for the majority of their energy needs, which can cause negative ecological and health impacts while limiting economic development. Bifacial photovoltaics present an alternative to diesel power. With high average latitudes, these communities show potential for large bifacial gains due to high albedo caused by snow and a high fraction of diffuse light; however, high-latitude conditions deviate from standard test conditions, with low average temperatures, light incident from many directions, and high average air masses, resulting in increased energy yield prediction uncertainty.

This thesis describes the performance of bifacial silicon heterojunction cells and modules under high-latitude operating conditions, including high angles of incidence and high air masses. Optical losses in the cell and module are described, and module characteristics are incorporated in DUET, the SUNLAB's energy yield prediction software, as an incidence angle modifier and air mass modifier.

The percentage change in energy yield when considering air mass is shown to increase with increasing latitude: for a single-axis-tracked installation, the annual difference in energy yield is 0.5% in a low-latitude location (33°N), and more than 2.5% in a high-latitude location (69°N). Air mass correction is demonstrated to improve energy yield prediction accuracy compared to the absence of spectral correction. This work improves energy yield prediction accuracy for high-latitude locations, facilitating adoption of solar energy in diesel-dependent remote communities in Canada and abroad.

Acknowledgements

Funding for the research work performed in this thesis has been provided by the National Science and Engineering Research Council (NSERC) through the Canada Graduate Scholarships-Master's (CGS-M), and by the Ontario Ministry of Training, Colleges, and Universities through the Ontario Graduate Scholarship (OGS). Natural Resources Canada provided data from their CanSIM network for results presented in chapter 5.

First, I would like to sincerely thank Dr. Karin Hinzer, for her consistent support and the incredible opportunities that she's provided me. Dr. Hinzer's positive attitude always encouraged me to challenge myself, and she made my Master's experience memorable. I would like to thank Dr. Chris Valdivia, whose guidance and infinite patience were incredibly valuable to me. I would also like to thank Dr. Henry Schriemer, for believing in me more than I sometimes believe in myself, and Dr. Mariana Bertoni, for welcoming me so warmly to Arizona. A giant thank you to the entire DEfECT lab team for making me feel at home. Lastly, I would like to thank my colleagues at the SUNLAB: Meghan Beattie and Dr. Matthew Wilkins, who answered all my questions; Annie Russell and Erin Tonita, who I worked with closely; and the other SUNLAB students, who kept things interesting.

I would like to recognize the support of close friends and family. Your positivity, understanding, and patience made this possible.

Declaration of Originality

The work presented in this thesis was performed by the author under the supervision of Dr. Karin Hinzer during the period of her M.A.Sc. studies. To the best of the author's knowledge, the results obtained in this thesis are original.

List of Publications

The following publications resulted from my research during the pursuit of my degree:

Conference Proceedings:

1. **M. R. Lewis**, E. M. Tonita, C. E. Valdivia, R-J. K. Obhi, J. Leslie, A. C. J. Russell, M. I. Bertoni, and K. Hinzer, "Modelling of Bifacial Silicon Heterojunction Solar Cells for Arctic Applications," in Proceedings of 46th IEEE Photovoltaic Specialists Conference (PVSC), Chicago IL, June 2019.
2. **M. R. Lewis**, A. C. J. Russell, C. E. Valdivia, J. E. Haysom, M. I. Bertoni, and K. Hinzer, "Impact of Air Mass on Energy Yield Calculation for Bifacial Silicon Heterojunction Photovoltaic Modules in High-Latitude Conditions," in 2020 IEEE 47th Photovoltaic Specialists Conference (PVSC), 2020.

Other Refereed Contributions:

3. **M. R. Lewis**, A. C. J. Russell, E. M. Tonita, C. E. Valdivia, J. E. Haysom, M. I. Bertoni, and K. Hinzer, "Impact of Bifacial Photovoltaic Cell Characteristics on Module Energy Yield in High Latitude Locations," in Photonics West 2020, San Francisco CA, February 2019. (Oral presentation).
4. **M. R. Lewis**, C. E. Valdivia, E. M. Tonita, R-J. K. Obhi, M. I. Bertoni, and K. Hinzer, "Effect of Encapsulant on Bifacial Silicon Heterojunction Solar Cell Operation for High Latitudes," in 29th International Photovoltaic Science and Engineering Conference (PVSEC), Xi'an, China, November 2019. (Oral presentation).
5. **M. R. Lewis**, E. M. Tonita, C. E. Valdivia, R-J. K. Obhi, J. Leslie, A. C. J. Russell, M. I. Bertoni, and K. Hinzer, "Angular Dependence of Bifacial Silicon Heterojunction Solar Cells for High Latitudes," in 19th International Conference on. Numerical Simulation of Optoelectronic Devices (NUSOD), Ottawa ON, July 2019. (Poster, first place prize winner).
6. **M. R. Lewis**, E. M. Tonita, C. E. Valdivia, R-J. K. Obhi, J. Leslie, A. C. J. Russell, K. Hinzer, and M. I. Bertoni, "Modelling of Bifacial Silicon Heterojunction Solar Cells for Arctic Applications," in 46th IEEE Photovoltaic Specialists Conference (PVSC), Chicago IL, June 2019. (Poster, area 4 prize winner).
7. **M. R. Lewis**, C. E. Valdivia, C. T. Li, A. C. J. Russell, H. P. Schriemer, K. Hinzer, "Bifacial Photovoltaic Module Energy Yield in Northern Canada," in 20th Photonics North Conference, Montreal QC, June 2018. (Poster, first place prize winner).

Table of Contents

List of Figures

List of Acronyms

a-Si:H	hydrogenated amorphous silicon
AM	air mass
AMM	air mass modifier
AOI	angle of incidence
ASTM	American Society for Testing and Materials
ASU	Arizona State University
c-Si	crystalline silicon
CWEC	Canadian Weather Year for Energy Calculation
DHI	diffuse horizontal irradiance
DNI	direct normal irradiance
EQE	external quantum efficiency
EVA	ethylene vinyl acetate
EY	energy yield
FWHM	full-width half-maximum
GHI	global horizontal irradiance
HIT	heterojunction with intrinsic thin-layer
IAM	incidence angle modifier
IEC	International Electrotechnical Commission
ITO	indium tin oxide
IQE	internal quantum efficiency
IR	infrared
LCOE	levelized cost of energy

PECVD plasma-enhanced chemical vapour deposition

PERC passivated emitter rear contact

PV photovoltaic

PVSC Photovoltaics Specialists' Conference

SCF spectral correction factor

SHJ silicon heterojunction

SMARTS Simple Model of the Atmospheric Radiative Transfer of Sunshine

TMY typical meteorological year

UV ultraviolet

List of Variables

Δ	phase difference
ϵ	sky clearness index
κ	Perez constant
λ	wavelength
ϕ	bifaciality factor
ψ	amplitude ratio
θ	zenith angle
c	speed of light
E	spectral irradiance
E_{g}	bandgap
EY_{AMM}	predicted energy yield with air mass correction
EY_{NoAMM}	predicted energy yield without air mass correction
EY_{NoSCF}	predicted energy yield without spectral correction
EY_{SCF}	predicted energy yield with spectral correction
FF	fill factor
h	Plank constant
Irr_{AMX}	irradiance of spectrum with air mass X
Irr_{ref}	irradiance of reference spectrum
Irr_{test}	irradiance of test spectrum
J	current
J_0	diode reverse saturation current
J_{d}	diode current
J_{mpp}	current at maximum power point
J_{ph}	photogenerated current
J_{sc}	short-circuit current
$J_{\mathrm{sc,AMX}}$	short-circuit current under spectrum with air mass X
$J_{\mathrm{sc,ref}}$	short-circuit current under reference spectrum
$J_{\mathrm{sc,test}}$	short-circuit current under test spectrum
k	Boltzmann constant
L	solar path length through the atmosphere
L_0	thickness of the atmosphere
n	ideality factor
P	power
P_{max}	maximum power
q	electron charge
R	reflectivity
R_{s}	series resistance

R_{sh}	shunt resistance
t	transmission
T	temperature
V	voltage
V_{mpp}	voltage at maximum power point
V_{oc}	open-circuit voltage

Chapter 1

Introduction

In Canada, nearly 200 000 people live in communities with no connection to the North American power grid [1]. Of these, approximately 100 000 people in 175 communities rely on diesel power for the majority of their energy needs [1]. In many locations, diesel fuel is transported by plane or by boat, resulting in high fuel costs and high electricity prices, up to $1.14/kWh [2], while the Canadian average is $0.14/kWh [3]. The government of Nunavut alone spends on average $60.5 million each year to subsidize diesel fuel [2].

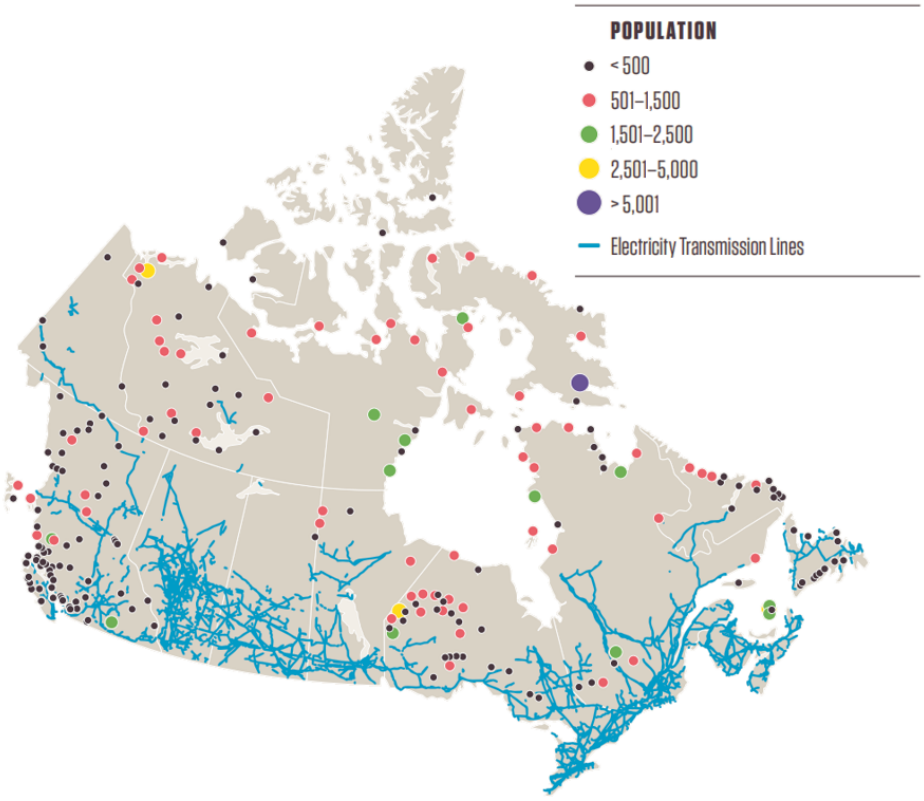

Figure 1.1: Map of diesel-dependent remote communities in Canada and electricity transmission lines. Adapted from [4]

Cost is not the only drawback of diesel-generated electricity; diesel fuel causes negative ecological and health impacts, including air pollution and fuel spills [5]. In addition, many remote communities operate near the maximum operating capacity of their diesel generator plants. This is a limiting factor for economic development, preventing, for example, the connection of new homes and upgrades to water treatment plants [4]. Considering the drawbacks of existing diesel infrastructure, alternative sources of energy such as solar and wind can provide considerable benefits, such as reduced costs and emissions [6].

Many projects, including renewable energy installations, face high installation and maintenance costs in remote communities; for example, the average solar installation price per kW in Nunavut is $\sim$1.6$\times$ that of Ontario [7]. Nevertheless, initial calculations demonstrate that solar energy is at grid parity in Nunavut and the Northwest Territories, with projected levelized costs as low as 24% of current electricity prices [8]. In fact, many pilot projects for establishing renewable energy sources in remote communities in Canada are currently underway, including solar module installations [9].

Diesel-reliant communities in Canada tend to be far north, with a population-weighted average latitude of approximately 60^{o}N. While northern summer irradiance is high, with 24 hours of sunlight in some locations, the winter irradiance is low. Therefore, other energy sources will be required, especially in winter, to complement solar energy production.

Arctic environmental conditions present some challenges to solar energy yield prediction, which is essential for determining project feasibility and securing funding. While photovoltaic cells and modules are typically tested at 25^{o}C under normally-incident light with a defined solar spectrum (ASTM AM1.5G), high-latitude conditions deviate from this standard, with low average temperatures, light incident from many directions, and high average air masses. These effects may not all be captured by typical energy yield prediction software, resulting in increased energy yield prediction uncertainty.

Bifacial photovoltaics, photovoltaic modules that absorb light on both the front and rear faces, show particular promise for Arctic operation due to its unique operating conditions. The average albedo (ground reflectivity) is high due to a high degree of snow cover, resulting in more ground-reflected irradiance, especially on the rear face. There is also a high proportion of diffuse light, resulting in high rear-side irradiance. These factors result in a high bifacial gain, the increase in energy yield due to light absorbed by the rear face. In addition, the average temperature is low, resulting in high photovoltaic cell efficiency [10].

While bifacial photovoltaics show promise for Arctic applications, characterizing their performance under high-latitude conditions will allow for more accurate energy yield prediction. This will reduce investment risk for bifacial photovoltaic systems in these communities, encouraging investment in Arctic photovoltaics and facilitating further solar power usage in remote northern communities in Canada.

1.1 Objective and Structure

This work's main objective is to characterize bifacial photovoltaic behaviour under high-latitude conditions, including high angles of incidence and high air mass spectra, to facilitate energy yield prediction.

This thesis includes publications that resulted from my research over the course of my Master's studies. There is some overlap between the publications.

Chapter 2 provides background information concerning the fundamentals of bifacial photovoltaics, a description of the modelling methods applied in this research, and details of the experimental methods used. Current generation in a solar cell and recombination mechanisms are described. The solar cell equivalent circuit is presented, and the effects of parasitic resistances are demonstrated. Bifacial photovoltaics, including silicon heterojunction modules (the subject of this thesis), the components of typical solar resource data, and air mass are defined. Simulation diagrams, describing how final results in chapters 4 and 5 were obtained, are presented.

Chapter 3 presents a conference proceeding submitted to the 46th IEEE Photovoltaics Specialists' Conference (PVSC). Methods for depositing thin-film samples at Arizona State University's Solar Power Lab are described. The design and performance of a silicon heterojunction solar cell with alternate texturing methods is modeled optically in SunSolve. Cell performance is analyzed at different angles of incidence. Different air mass spectra are applied at a range of angles, and high air mass performance is analyzed.

Chapter 4 presents the final draft of a conference proceeding submitted to the 47th IEEE Photovoltaics Specialists' Conference (PVSC). It describes the modelling methods applied to obtain a module's incidence angle modifier and air mass modifier, and demonstrates the impact of the air mass modifier on energy yield predictions in three North American cities. The air mass modifier is demonstrated to be more significant in high latitude locations due to higher average air masses.

Chapter 5 presents an early draft of an article. The air mass modifier is presented again; its impact with respect to latitude is demonstrated for eight locations. In accordance with previous results, the air mass modifier impact is shown to increase with increasing latitude. Spectral data from the CanSIM network, reconstructed by a SolarSIM-G, is used to generate a spectral correction factor. The spectral correction factor is compared to the air mass modifier, and the impact of both modifiers on energy yield are compared. The air mass modifier is shown to improve agreement with the spectral correction factor on an annual basis. More work is required to obtain an accurate approximation of the spectral correction factor without spectral data.

Chapter 6 is the conclusion of this work.

1.2 Copyright Permissions

Chapter 2

Background

2.1 Solar Photovoltaic Operation Principles

2.1.1 Current Generation in a Solar Cell

When light shines on a solar cell, the absorption of a photon promotes an electron from the valence band to the conduction band, forming an electron-hole pair. The electron and hole are subsequently separated by the solar cell, then flow out of the cell and generate current.

In order for a photon to generate an electron-hole pair, it must have energy above the semiconductor bandgap, E_g. If the photon energy is higher than the bandgap, carriers (electrons and holes) are excited beyond the band edge and quickly thermalize back to the band edge; the additional energy is lost as heat. If the photon energy is below the bandgap, the light passes through the semiconductor and does not generate an electron-hole pair (figure 2.1).

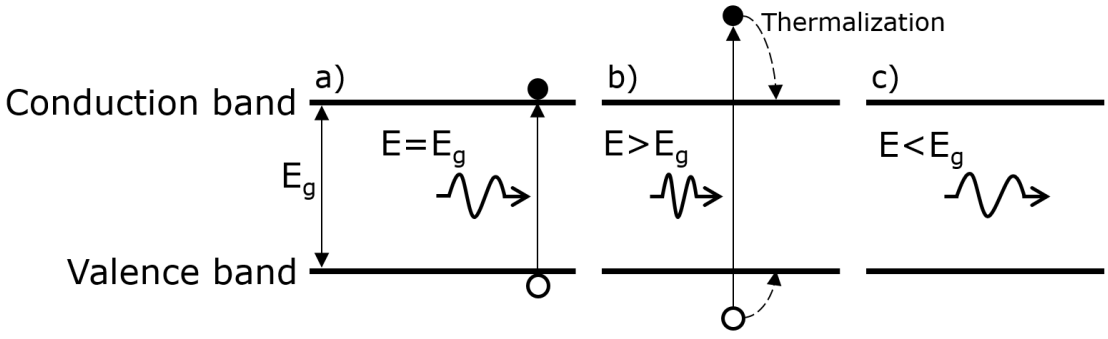

Figure 2.1: Electron-hole pair generation in a solar cell, with a) photon energy equal to the bandgap energy, b) photon energy greater than the bandgap energy, and c) photon energy below the bandgap energy (no electron-hole pair is generated).

The ASTM G-173-03 standard [12], defines the standard solar spectrum with variable spectral irradiance between 300 – 4000 nm. The trade-off between thermalization and transparency losses with respect to bandgap results in a maximum possible efficiency that can be obtained under

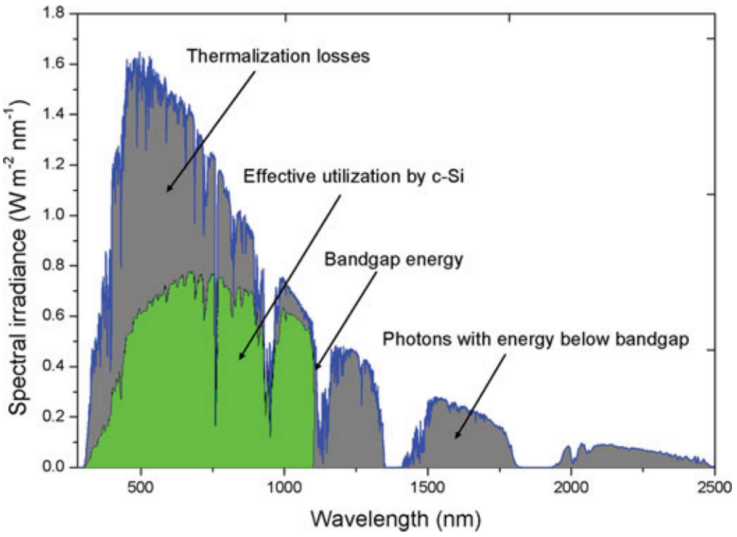

Figure 2.2: Spectral irradiance wavelengths effectively used by crystalline silicon (c-Si) highlighted in green. Reference solar spectrum in grey [11].

the standard solar spectrum, derived by Shockley and Queisser in 1961 and called the Shockley-Queisser limit [13]. For the bandgap of crystalline silicon (c-Si), the Shockley-Queisser limit under the standard AM1.5G spectrum is approximately 32% [13].

2.1.2 Recombination

Recombination is the process of an electron dropping from the conduction band to the valence band, thereby eliminating an electron-hole pair and reducing solar cell efficiency. There are three main types of recombination in a bulk semiconductor: radiative recombination, Auger recombination, and Shockley-Read-Hall (or trap-assisted) recombination (figure 2.3) [14].

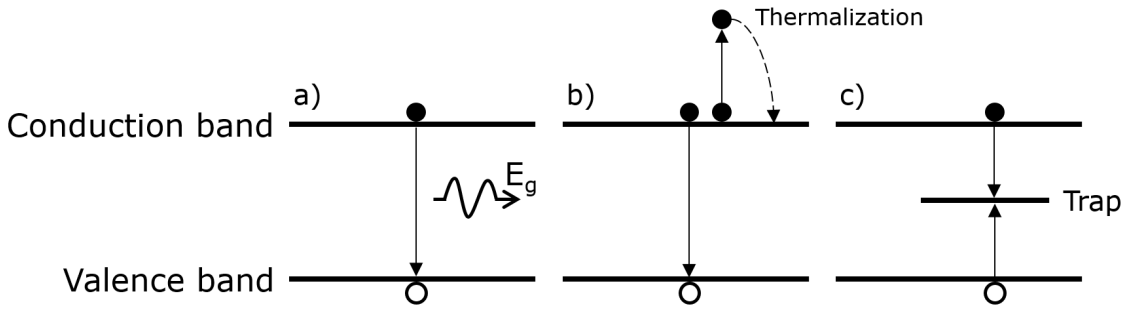

Figure 2.3: Types of recombination in a semiconductor bulk: a) radiative band-to-band recombination, b) non-radiative Auger recombination, and c) Shockley-Read-Hall (trap-assisted) recombination.

In radiative recombination (the inverse process to photon absorption), the electron and hole recombine and emit a photon with the bandgap energy, E_g. Since the photon energy is so near the bandgap, these photons are only weakly absorbed by the semiconductor and are likely to escape the solar cell. Radiative recombination dominates in direct bandgap semiconductor materials, such

as GaAs. In indirect bandgap semiconductor materials, such as silicon, a phonon is required for the radiative recombination process, and radiative recombination is therefore lower [15].

Non-radiative Auger recombination is a similar process, but rather than releasing a photon, the energy is transferred to another carrier, increasing its energy. The energy is then lost to heat as the carrier relaxes to the band edge. Auger recombination increases as the carrier concentration increases because it requires three carriers, so it is more important in heavily doped materials or under high concentrations of sunlight [15]. These first two recombination mechanisms are considered unavoidable, because they are a basic property of the semiconductor.

Shockley-Read-Hall (trap-assisted) recombination is caused by defects in the semiconductor, for example, dangling bonds, lattice dislocations, or impurities. Defects create a trap state (a localized defect level), in the bandgap of the semiconductor. This defect level can assist recombination with another carrier that is also trapped at the defect level. Shockley-Read-Hall recombination is related to the quality of the semiconductor, and may be reduced by improving the semiconductor material quality through improved fabrication processes.

Recombination can also occur at the semiconductor's surface due to defects at the surface and the presence of dangling bonds. At the surface, the crystal lattice is interrupted, leaving empty states in the surface atoms' valence bands called dangling bonds [16]. Surface recombination is a similar process to trap-assisted recombination, but the surface presents a near-continuous number of states which results in a near-infinite sink for carriers. Surface recombination can be quantified using the surface recombination velocity, in units of centimeters/second. If there is no surface recombination, there is no movement of carriers towards the surface, so the surface recombination velocity is assumed to be 0 cm/s.

Passivation reduces the surface recombination rate of the solar cell, resulting in longer carrier lifetimes [17]. There are two types of surface passivation: field-effect passivation and chemical passivation. Field-effect passivation creates a layer of fixed charges at the surface, repelling minority carriers and preventing them from reaching the surface and recombining. Chemical passivation reduces defects by saturating the dangling bonds at the surface, usually with hydrogen atoms, so that there is no longer a trap state with which to recombine. Most surface passivation methods, such as SiN_x:H deposition, will employ a combination of field-effect and chemical passivation in order to increase carrier lifetimes [17].

Practically speaking, these recombination mechanisms make it difficult to achieve the Shockley-Queisser efficiency limit described in 2.1.1.

2.1.3 Solar Cell Equivalent Circuit

An ideal solar cell can be represented by a current source in parallel with a single diode, as represented in the circuit diagram in figure 2.4. J_{ph} represents the photogenerated current in the cell caused by incident illumination, and increases with increased incident solar irradiance [18]. While a single diode is used in this model, a second diode in parallel with the first can also be used to represent junction recombination in the cell.

Applying Kirchoff's current law to the circuit, the current, J, of the solar cell becomes:

$$J = J_{ph} - J_d = J_{ph} - J_0 \left(e^{\frac{qV}{nkT}} - 1 \right) \tag{2.1}$$

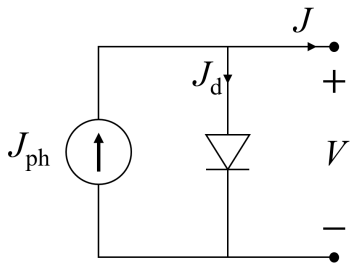

Figure 2.4: Simplified solar cell equivalent circuit. J_{ph}: photogenerated current. J_d: diode current. J: solar cell current. V: solar cell voltage.

where J_{ph} is the photogenerated current in the cell, J_d is the diode current, J_0 is the diode reverse saturation current, q is the electron charge, V is the cell voltage, n is the ideality factor, k is the Boltzmann constant, and T is the absolute temperature [18]. The ideality factor represents the non-ideal behaviour of the solar cell due to second-order effects in the cell. As we can see from equation 2.1, if there is no light incident on the solar cell ($J_{ph} = 0$), the cell is simply a diode.

This equation results in a current-voltage curve, or J-V curve, as shown in figure 2.5:

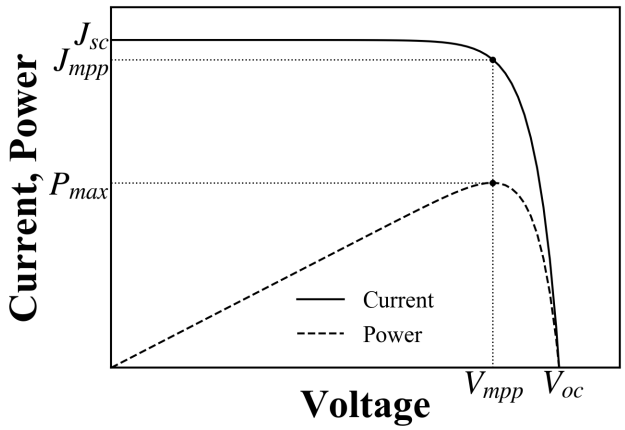

Figure 2.5: J-V curve and power curve of an ideal solar cell. J_{sc}: short-circuit current. J_{mpp}: current at maximum power point. V_{oc}: open-circuit voltage. V_{mpp}: voltage at maximum power point. P_{max}: maximum power.

As the light incident on the cell increases, and therefore the short-circuit current (J_{sc}) increases, the J-V curve shifts up along the y-axis, increasing the power generated by the cell.

The maximum power point of the solar cell, P_{max}, shown in figure 2.5, defines the fill factor FF:

$$FF = \frac{P_{max}}{J_{sc}V_{oc}} = \frac{V_{mpp}J_{mpp}}{J_{sc}V_{oc}} \tag{2.2}$$

where FF is the fill factor, P_{max} is the maximum power of the cell, J_{sc} is the short-circuit current, V_{oc} is the open-circuit voltage, V_{mpp} is the voltage at the maximum power point, and J_{mpp} is the current at the maximum power point.

One way of describing the fill factor is the ratio of the area of two rectangles: one outlined by the

maximum power point's current and voltage (numerator in equation 2.2), and the other outlined by the short-circuit current and open-circuit voltage (denominator in equation 2.2). The higher the fill factor, the better the quality of the solar cell; the fill factor is reduced by the series resistance, R_s, and the shunt resistance, R_{sh}.

To demonstrate that the solar cell is not perfectly ideal, these two resistances can be added to the solar cell diagram (figure 2.6). The series resistance represents the resistance of the of the solar cell material, the contact resistance between the metal contacts and the silicon, and the resistance of the metal contacts [18]. The shunt resistance represents alternative current paths, including defect-assisted recombination and edge shunting around the perimeter of the device [19]. Both of these resistances (low R_{sh} and high R_s) reduce the fill factor, and therefore the maximum power of the solar cell.

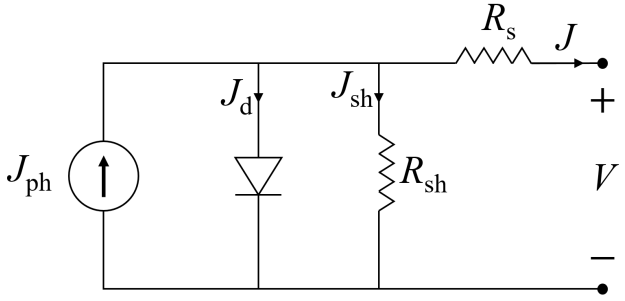

Figure 2.6: Simplified solar cell equivalent circuit with parasitic resistances. J_{ph}: photogenerated current. J_d: diode current. J_{sh}: shunt current. J: solar cell current. R_{sh}: shunt resistance. R_s: series resistance. V: solar cell voltage.

We can apply Kirchoff's current law to new circuit diagram in figure 2.6, and the J-V equation becomes:

$$J = J_{ph} - J_d - J_{sh} = J_{ph} - J_0 \left(e^{\frac{q(V+JR_s)}{nkT}} - 1 \right) - \frac{V + JR_s}{R_{sh}} \tag{2.3}$$

where J is the solar cell current, J_{ph} is the photogenerated current in the cell, J_d is the diode current, J_{sh} is the shunt current, J_0 is the diode reverse saturation current, q is the electron charge, n is the ideality factor, k is the Boltzmann constant, T is the absolute temperature, R_s is the series resistance, R_{sh} is the shunt resistance, and V is the cell voltage [18]. When these resistances are incorporated, the J-V curve is changed and FF decreases, as shown in figure 2.7.

The slope of the dashed lines in figure 2.7a and b can be used to approximate the series and shunt resistances, respectively.

When the photocurrent is low, the losses due to shunt resistance become more important because the current through the shunt resistance pathways (J_{sh}) represents a larger proportion of the overall generated current. When the photocurrent is high, the losses due to series resistance become more important, since the loss in the resistor ($P = J^2 R_s$) increases quadratically with current. If series resistance becomes too high or shunt resistance becomes too low, the cell will operate as a resistor.

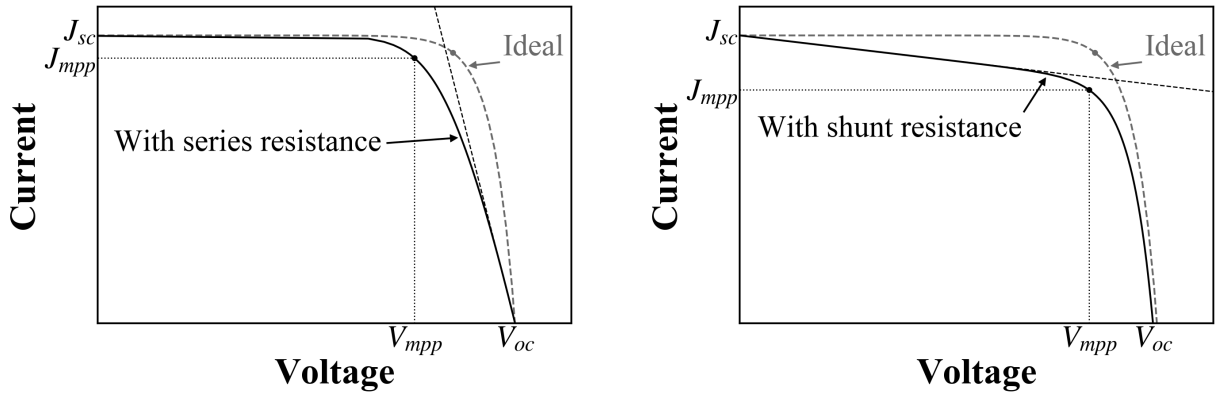

Figure 2.7: *J-V* Curves of an ideal solar cell (grey) and a solar cell with a) series and b) shunt resistance (black). Maximum power points indicated. J_{sc}: short-circuit current. J_{mpp}: current at maximum power point. V_{oc}: open-circuit voltage. V_{mpp}: voltage at maximum power point.

2.1.4 Quantum Efficiency

Quantum efficiency is a measurement of the quality of a solar cell, defining the efficiency with which a solar cell converts photons into current. Quantum efficiency is dependent on wavelength, λ: for a given photon energy level, the external quantum efficiency (EQE) is the ratio of charge carriers that are collected by the solar cell to the number of photons incident on the solar cell. If all of the photons incident on the solar cell at a given wavelength are absorbed and generate an electron-hole pair that is then collected as current, the EQE at that wavelength is 1.

$$EQE(\lambda) = \frac{\#\text{ electrons collected}(\lambda)}{\#\text{ incident photons}(\lambda)} \tag{2.4}$$

The internal quantum efficiency (IQE) is the ratio of charge carriers collected by the solar cell to the number of photons that are absorbed by the cell:

$$IQE(\lambda) = \frac{\#\text{ electrons collected}(\lambda)}{\#\text{ absorbed photons}(\lambda)} = \frac{EQE(\lambda)}{1 - t(\lambda) - R(\lambda)} \tag{2.5}$$

where t is the transmission through the solar cell and R is the reflection from the front of the cell. While EQE accounts for transmission and reflection losses, IQE only defines losses that are internal to the solar cell, such as recombination. By definition, the EQE is always less than the IQE. By measuring the EQE, the reflectance, and the transmission of a solar cell, the IQE can be calculated.

The spectral responsivity (SR) is the fraction of available irradiance that is converted into current, in A/W. The spectral responsivity of a cell or module can be determined from the EQE as:

$$SR(\lambda) = \frac{q\lambda}{hc} EQE(\lambda) \tag{2.6}$$

where q is the elementary charge in C, λ is the wavelength in m, h is the Plank constant in J·s, c is the speed of light in m/s, and EQE is the external quantum efficiency of the module. Spectral responsivity is lower at short wavelengths, and higher at long wavelengths. This is due to the additional power per photon at short wavelengths, which cannot be used by the solar cell and is lost through thermalization. Typical spectral responsivity and external quantum efficiency curves for the silicon heterojunction module studied in this work are shown in figure 2.8.

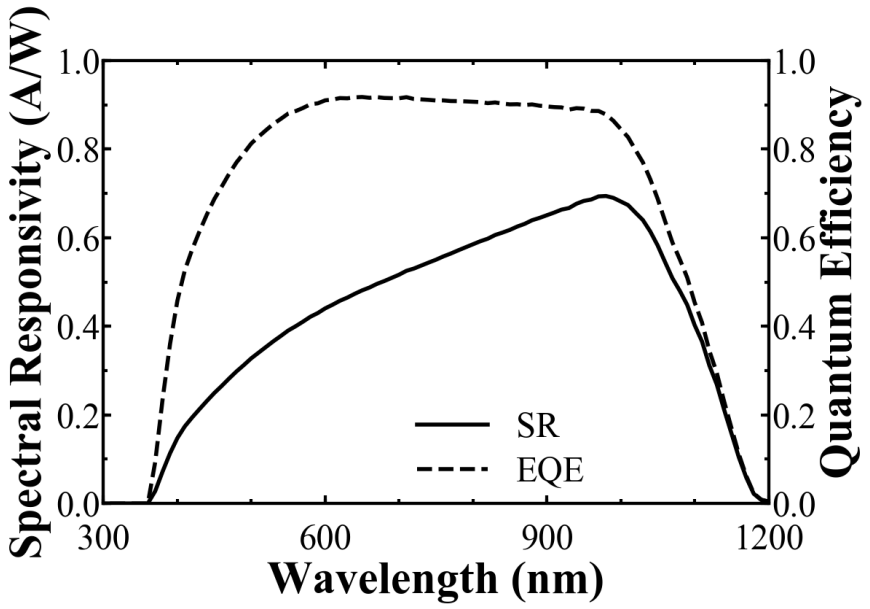

Figure 2.8: Spectral response (SR) and external quantum efficiency (EQE) of bifacial silicon heterojunction module.

If the EQE, and therefore the SR, is known, the short-circuit current density can be calculated for an incident spectrum as:

$$J_{sc} = \int SR(\lambda)E(\lambda)d\lambda \tag{2.7}$$

where J_{sc} is the short-circuit current density in A/m^2, SR is the spectral response in A/W, and E is the incident spectral irradiance in W/m^2/nm. The J_{sc} is typically expressed in mA/cm^2 for single cells.

2.1.5 Bifacial Photovoltaics

Unlike monofacial solar panels, which absorb light only on the front face, bifacial panels absorb light from both the front and rear faces. This results in an increase in energy yield due to the additional irradiance on the rear face, primarily from diffuse and ground-reflected light (figure 2.9).

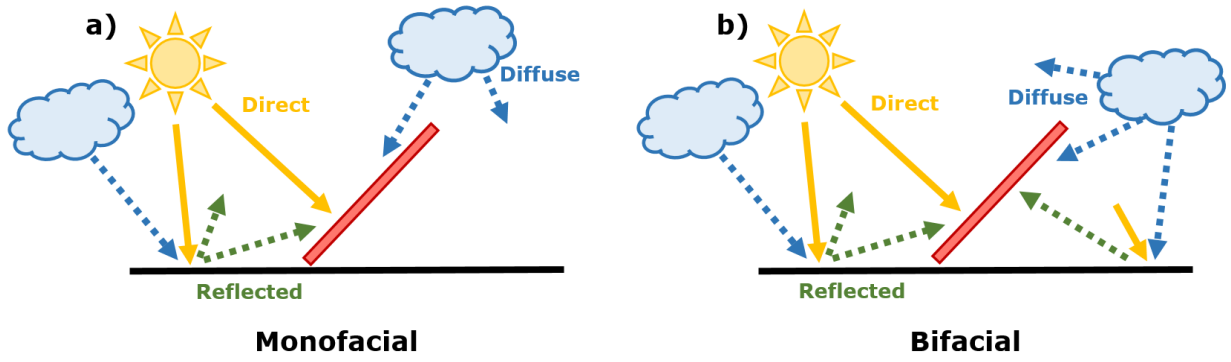

Figure 2.9: Sources of irradiance for a) monofacial and b) bifacial solar panels.

The increase in energy yield is called the bifacial gain, and is defined as:

$$Bifacial\ Gain = \frac{EY_{bi} - EY_{mono}}{EY_{mono}} \tag{2.8}$$

where EY_{bi} is the energy yield for a bifacial module, and EY_{mono} is the energy yield of a monofacial module under the same site and weather conditions. Bifacial installations have demonstrated gains exceeding 30% over monofacial modules [20].

Due to differences in cell design (for example, different metallization patterns), the rear face of a bifacial cell or module is less efficient than the front face. This difference in efficiency is defined by the bifaciality factor, ϕ, the ratio of short-circuit current generated by the rear face to the short-circuit current generated by the front face under standard test conditions:

$$Bifaciality\ Factor,\ \phi = \frac{J_{sc,rear}}{J_{sc,front}} \tag{2.9}$$

where ϕ is the bifaciality factor, $J_{sc,rear}$ is the current collected from the rear module face, and $J_{sc,front}$ is the current collected from the front module face. According to a new standard describing bifacial cell characterization, IEC60904-1-2 [21], bifacial short-circuit current is proportional to the sum of the incident irradiance on both the front and rear faces, with the rear-side irradiance de-rated by the bifaciality factor [22].

High-efficiency bifacial modules (such as silicon heterojunction and passivated emitter rear contact, or PERC, cells) require a minimal increase in cost over high-efficiency monofacial modules, as they use similar fabrication methods [23]. Maintenance cost for bifacial installations is expected to be less than monofacial installations, due to the reduced number of panels required for the same power output. Together with the increase in energy yield, these factors greatly reduce the levelized cost of energy (LCOE) of bifacial systems compared to monofacial for most locations [24]. Therefore, bifacial photovoltaics are projected to make up 40% of the crystalline silicon market share by 2028 [25].

However, bifacial photovoltaics are still an emerging technology, and there is some uncertainty in modelling bifacial gain [23]. Many factors can affect the bifacial gain, including surface albedo, diffuse light fraction, racking configuration, and row spacing [23]. This uncertainty may slow future

adoption of bifacial modules. Further improvements in modelling technology and additional field test data are required to provide key stakeholders greater confidence in adopting bifacial technology.

2.1.6 Silicon Bifacial Heterojunction Solar Modules

Silicon heterojunction solar cells are high-efficiency solar cells that incorporate thin-film hydrogenated amorphous silicon (a-Si:H) layers on the front and rear faces. The first modern silicon heterojunction (SHJ) solar cell was invented in 1992 by Sanyo [26]. They coined the term HIT cell, or heterojunction with intrinsic thin-layer, to describe the multilayer a-Si:H structure with a thin intrinsic layer between the c-Si and the doped a-Si:H. Today, the world record of efficiency for a crystalline silicon solar cell is held by a heterojunction cell, at 26.7% [27].

The typical silicon heterojunction module design is shown in figure 2.10. This includes a c-Si wafer, pyramidally textured for light-trapping, with layers of intrinsic and doped a-Si:H and indium tin oxide (ITO) on the front and rear faces. The PN junction of the cell is at the front, between the c-Si and p+ a-Si:H layers. For the full module, there are also ethylene vinyl acetate (EVA) encapsulant and glass layers on both faces. Heterojunction cells have a high bifaciality due to their symmetry between the front and rear faces [28].

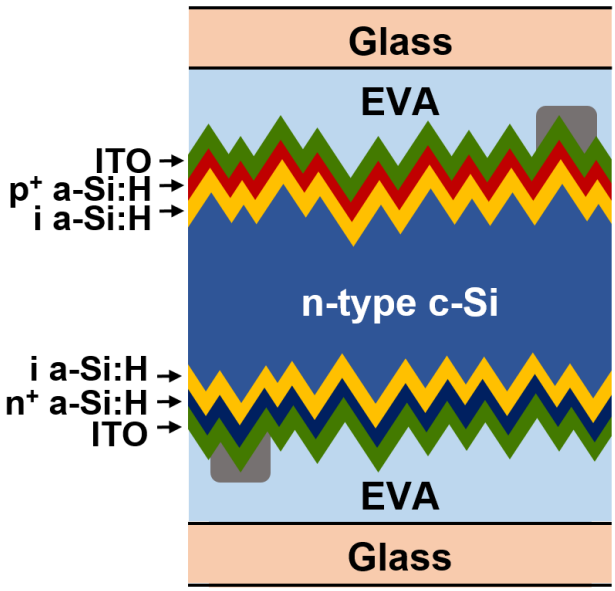

Figure 2.10: Cross-section of typical silicon bifacial heterojunction module design. c-Si: cyrstalline silicon. a-Si:H: hydrogenated amorphous silicon. ITO: indium tin oxide. EVA: ethyl vinyl acetate.

One advantage of SHJ design is the high-quality passivation provided by the a-Si:H layers, resulting in high open circuit voltage, V_{oc} (and high efficiency) [29]. The a-Si:H layers provide chemical passivation by hydrogenating the c-Si dangling bonds, while the doped a-Si:H layers provide field-effect passivation by repelling minority carriers [30].

In addition, the a-Si:H layers allow for lower temperature deposition than standard aluminium back-surface-field c-Si cell fabrication processes, reducing the cost and energy payback time of the solar module [31]. One drawback to a-Si:H is its optical absorption in the short-wavelength range,

only a fraction of which can be collected, causing a reduction in the J_{sc} by reducing the amount of light that is absorbed in the c-Si wafer [32].

The ITO layers allow for lateral carrier conduction on both cell faces while also acting as anti-reflection coatings. ITO is highly conductive, with typical resistivity in the 10^{-5} to 10^{-4} Ω·cm range [33]. This conductive layer is required because the a-Si:H layers are thin and highly resistive, so the carriers cannot be conducted laterally through the a-Si:H layer to the contact [28]. The ITO thickness is usually set to 75 nm to act as an anti-reflection coating with a reflectance minimum at 600 nm (the peak of the solar spectrum) due to destructive interference in the thin film. In a typical anti-reflection coating, the coating thickness is one-quarter of the desired wavelength of the reflectance minimum, so the beam travels exactly half its wavelength after reflecting from the second interface.

The encapsulation layers (EVA and glass) help to protect the cell from the environment, including moisture and dust, allowing modules to have a standard 25-year service life [34]. While module efficiency decreases over time, encapsulation helps to mitigate environmental effects on the cell. Encapsulation also creates a structure to support the solar cells: EVA provides adhesion between front and rear glass sheets, and the glass offers structural support. While necessary, the encapsulation process reduces module efficiency due to parasitic absorption in the EVA and glass (especially in the UV range) and reduces module performance due to increased reflectivity at the glass-air interface, as shown in Chapter 4.

2.1.7 Components of Solar Irradiance

Weather data, such as the Canadian Weather Year for Energy Calculation (CWEC) or Typical Meteorological Year (TMY) files, include direct, diffuse, and global irradiance data. The direct normal irradiance (DNI) is direct radiation that is incident on a plane normal to the sun's beam (figure 2.11a). It typically includes circumsolar radiation, which is radiation measured within ±2.5° of the center of the sun [35]. Diffuse horizontal irradiance (DHI) is irradiance that has been scattered by the atmosphere and therefore comes from all directions, except directly from the sun. It is measured on a horizontal plane parallel to the ground, as shown in figure 2.11b. Global horizontal irradiance (GHI) is the total irradiance incident on a horizontal surface, including both direct and diffuse light.

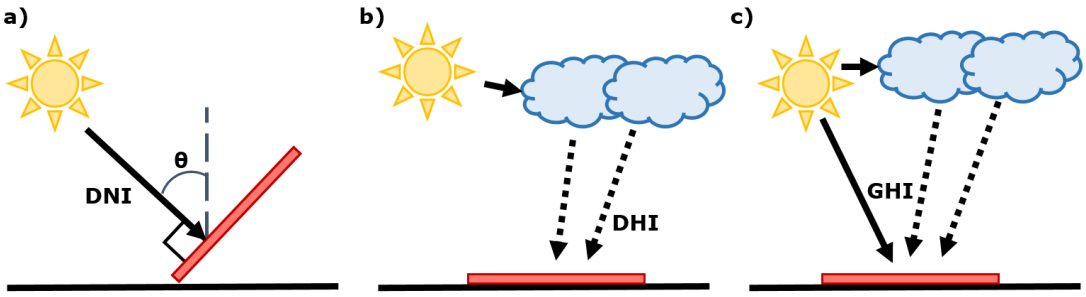

Figure 2.11: Diagram of a) direct irradiance, b) diffuse irradiance, and c) global irradiance. DNI: direct normal irradiance. GHI: global horizontal irradiance. DHI: diffuse horizontal irradiance.

The three terms are related by the following equation:

$$GHI = DHI + DNI\cos(\theta) \tag{2.10}$$

where θ is the solar zenith angle, the angle from a vertical line perpendicular to the ground to the sun's position in the sky.

These three components of solar radiation are readily available for many locations across the globe, and are commonly used by energy resource models, such as the DUET model described in section 2.2.3.

2.1.8 Air Mass

The air mass is the ratio of the path length of sunlight through the atmosphere to the effective thickness of the atmosphere (see figure 2.12). When the sun is directly overhead, the air mass is 1. The solar spectrum that is incident on the outside of the earth's atmosphere is called air mass zero (AM0), since it has not passed through the atmosphere at all. The sun emits radiation over a wide wavelength range, and the AM0 spectrum closely resembles the shape of blackbody radiation with a temperature of ~5800 K [36].

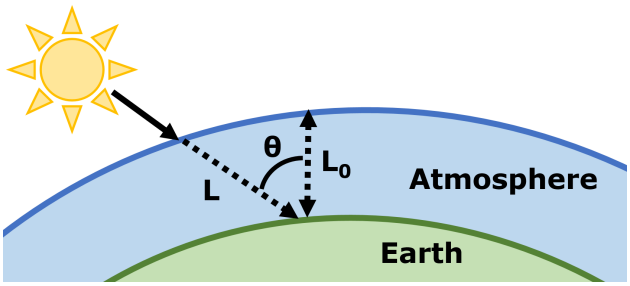

Figure 2.12: Diagram of sun path length through the atmosphere for air mass calculation. L: sun's path length through the atmosphere. L_0: thickness of the atmosphere. θ: zenith angle.

$$Air\ Mass = \frac{\text{Path length, } L}{\text{Thickness of atmosphere, } L_0} = \frac{1}{\cos(\theta)} \tag{2.11}$$

While equation 2.11 is sufficient for most cases, it deviates from the correct air mass value at high zenith angles. Due to the gradual difference in air density, and therefore refractive index, as a function of height, there is a slight bend in the sunlight's path as it approaches the earth. This requires a small correction in the air mass calculation as follows [37]:

$$Air\ Mass' = \frac{1}{\cos(\theta) + 0.50575(96.07995 - \theta)^{-1.6364}} \tag{2.12}$$

As light travels through the atmosphere, portions of the spectrum are absorbed by molecules in the atmosphere, including water, ozone, oxygen, and carbon dioxide, resulting in a change to the shape and overall intensity of the solar spectrum. The American Society for Testing and Materials

(ASTM) has developed a standard spectrum to represent solar radiation, G173-03 [12], which assumes an air mass of 1.5 (zenith angle of 48°). However, this standard is meant to represent the average solar irradiance spectrum for a typical location. Atmospheric conditions, including the weather and atmospheric pollutants, as well as the sun's position in the sky, change the irradiance spectrum.

If the sun is low in the sky, and therefore air mass is high, the UV portion of the solar spectrum is reduced due to the attenuation of UV wavelengths by atmospheric scattering (see figure 2.13) [38]. This also reduces the overall intensity of the incident irradiance (see inset, figure 2.13). This changing spectral shape will affect module efficiency, as explored in chapters 4 and 5.

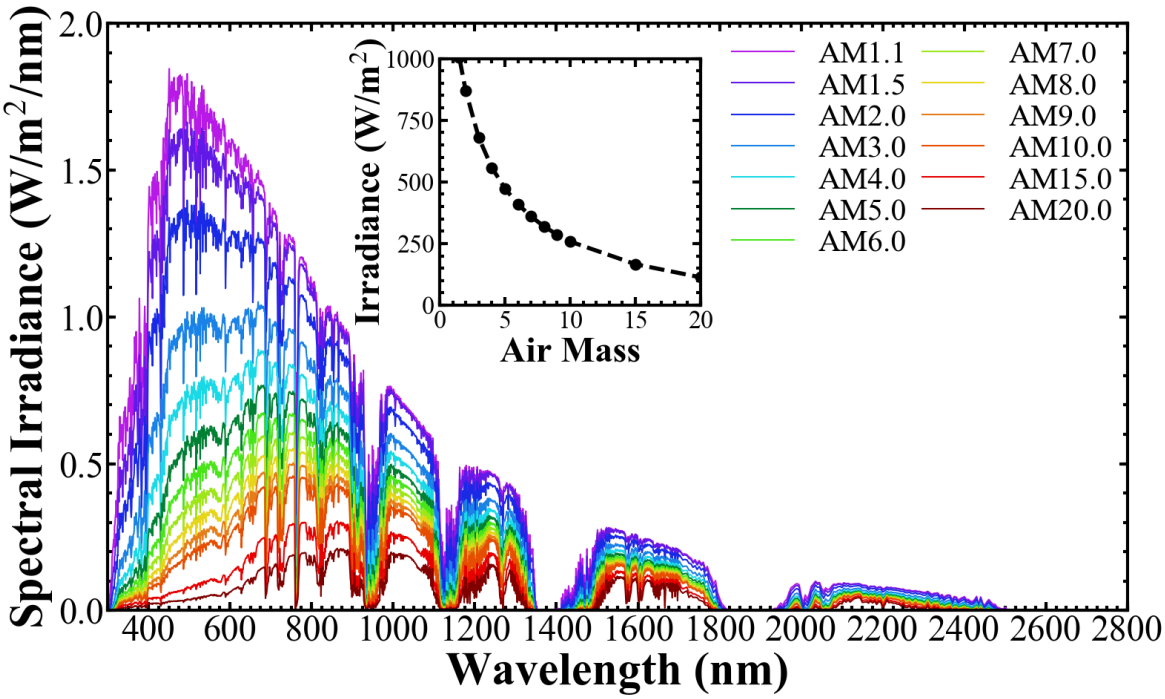

Figure 2.13: Spectral irradiance for air masses from AM1.1 to AM20 generated by SMARTS. Inset: total irradiance for air mass spectra for AM1.1 to AM20.

2.2 Energy Yield Prediction: Software, Modelling Methods, and Instrumentation

2.2.1 SunSolve

SunSolve is a Monte Carlo online ray-tracing program by PVLighthouse that calculates the optical and electrical performance of a solar module or cell under a given illumination source [39]. It combines thin-film optics with Beer-Lambert absorption to determine optical losses in the device under test. Each device is defined as a layer stack of materials and thin films, each with their own complex refractive index, thickness, and texture morphology.

The ray-tracing algorithm generates a number of rays, called a ray packet, assigning each a wave-

length, an intensity, a direction, and a location, based on user inputs. Each light ray proceeds in a straight line until it intersects with the cell or module surface. At the interface, reflectance, transmittance, and absorptance are calculated based on the ray's wavelength, the refractive index of the materials on either side of the interface, and the thin films between them. The intensity of the ray is reduced by the absorptance of the thin films, and it is then either reflected or transmitted based on a random calculation weighted by the calculated reflectance and transmittance. The ray is then assigned a new direction based on the interface's scattering model and whether the ray is transmitted or reflected. If the ray passes through an optically thick absorbing layer, the intensity is reduced by Beer's law. The transmission, reflection, and absorption in each layer are then summed for all of the rays in the ray packet and averaged for the entire ray packet. The average of all of the ray packets are then returned to the user.

The optical losses in each layer with respect to wavelength of a silicon heterojunction bare cell and a silicon heterojunction module are discussed in chapters 3 and 4, respectively. This model does not currently include drift/diffusion or temperature effects.

2.2.2 Simple Model of the Atmospheric Radiative Transfer of Sunshine

Simple Model of the Atmospheric Radiative Transfer of Sunshine (SMARTS) is a computer software that simulates solar irradiance spectra under clear-sky conditions [40]. It uses various inputs to describe the atmospheric conditions for which irradiance spectra are calculated. SMARTS can calculate direct, diffuse, global, and circumsolar irradiance on any horizontal or tilted surface for wavelengths from 280 - 4000 nm. Spectral resolution is 0.5 nm for 280-400 nm, 1 nm for 400-1750 nm, and 10 nm for 1750-4000 nm. It has been subject to extensive validation and is used to define the ASTM G-173-03 AM1.5G standard spectrum (see figure 2.14) [12]. In this work, SMARTS was used to generate reference spectra and spectra with varying air mass.

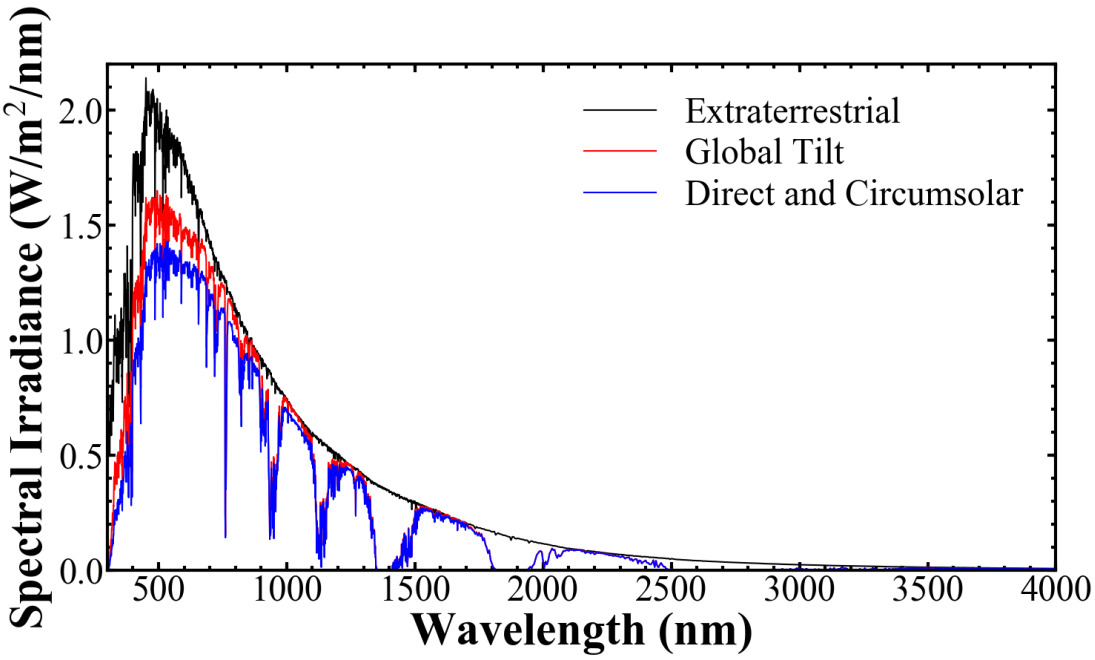

Figure 2.14: Reference spectra defined by ASTM G173-03, generated by SMARTS.

2.2.3 DUET

DUET is the SUNLAB's energy yield prediction software for bifacial PV, which incorporates elements of a 3D view-factor model with ray-intersection shading checks for system elements, such as racking and torque tubes [41]. The Python-based model takes weather files, such as Canadian Weather Year for Energy Yield Calculation (CWEC) or Typical Meteorological Year (TMY) files, as input, along with system parameters (e.g. module orientation, racking, spacing), and module characteristics (e.g. wiring and bypass diode configuration, responsivity). The model then calculates monofacial and bifacial energy yield for each timestamp in the weather file.

DUET divides irradiance into three sources: direct solar radiation, diffuse sky dome radiation, and ground-reflected radiation. The diffuse sky dome (see figure 2.15) is found based on the Perez 1993 model [42], a measurement-based mathematical model that calculates luminance distribution. The model calculates sky clearness and sky brightness (as described in [42] and [43]) from direct normal and diffuse horizontal irradiance, then finds the luminance distribution based on these factors and the sun's location in the sky.

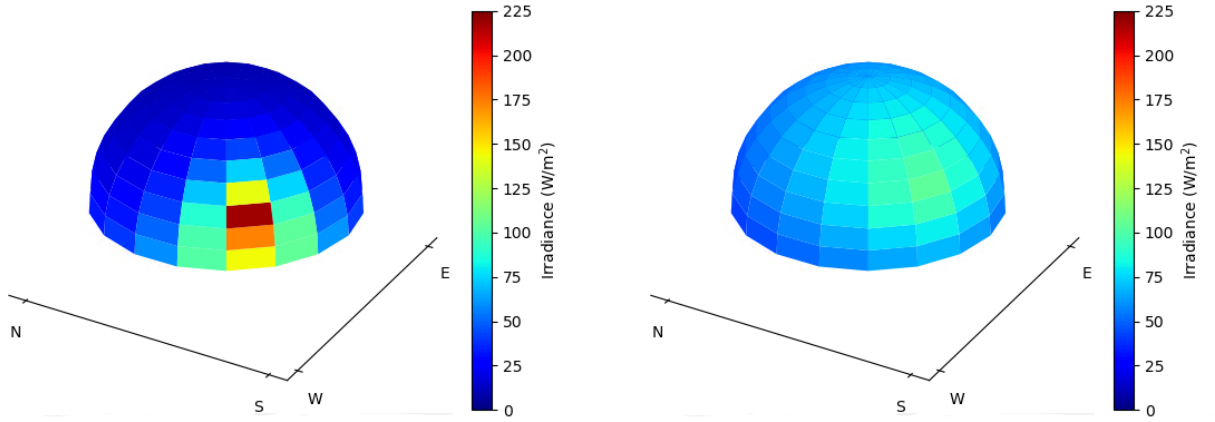

(a) **(b)**

Figure 2.15: Diffuse sky dome irradiance, divided into sky patches, for a a) sunny and a b) cloudy timestamp, generated in DUET. Sunny: GHI = 410 W/m^2, DNI = 716 W/m^2, DHI = 77 W/m^2. Cloudy: GHI = 201 W/m^2, DNI = 0 W/m^2, DHI = 201 W/m^2.

DUET sections the diffuse sky dome, ground, and panel under analysis (front and rear) into patches. Each pair of patches includes an irradiance source and an irradiance target (sky to ground, sky to panel, and ground to panel), and a ray connecting the center of these patches is checked for intersection with scene shading elements, such as the torque tube and posts. If a target patch is found to be shaded from a source patch, the irradiance incident on the receiving patch from the irradiant patch is set to zero.

For each set of patches (sky to ground, sky to panel, and ground to panel), the model calculates the view factor connecting every radiant patch to every target patch, and calculates the incident irradiance on each target patch from each irradiant patch. The sum of all irradiant patch contributions determines the total irradiance incident on each target patch. In this calculation, the ground patches act first as target patches, receiving irradiance from the diffuse sky dome and the sun. The model then multiplies the total irradiance on each ground patch by the ground albedo

(ground reflectance between 0 and 1) before performing the ground-to-panel irradiance calculation. The ground-reflected, diffuse, and direct irradiance on each panel patch is then summed to find the total panel patch irradiance, as shown in figure 2.16.

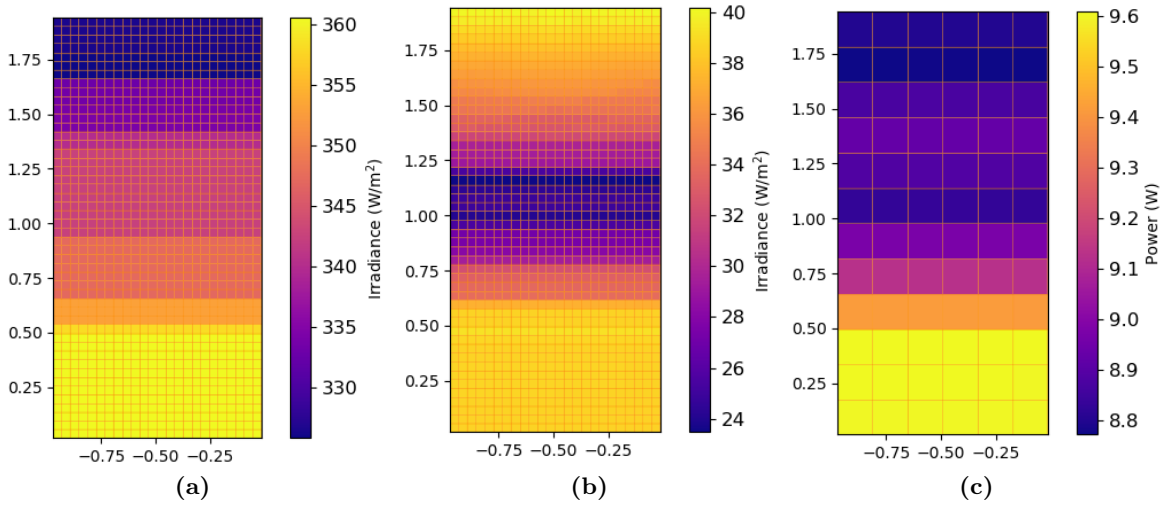

Figure 2.16: a) Front-incident irradiance, b) rear-incident irradiance, and c) total cell power for a bifacial module in DUET. Generated for a single-axis-tracked module in Cambridge Bay, NU, on a sunny timestamp. Shading from torque tube can be observed in the rear-side irradiance.

In this way, the sum of incident irradiance from all sources, including directly from the sun, from each sky patch, and from each ground patch, is found for each panel patch. The total incident irradiance on each cell is found by summing the total irradiance on the cell patches. For bifacial energy yield calculations, the model de-rates the rear-side irradiance by the bifaciality factor, then adds it to the front-side irradiance. This irradiance is used to determine each cell's photogenerated current, and the full J-V curve is calculated following the 1-diode model, adjusted for temperature. Cell J-V curves are summed depending on the module's internal wiring architecture to determine full module power. The maximum power point is multiplied by the timestamp duration to find module energy yield for that timestamp.

This process is repeated for each timestamp, and the per-timestamp energy yield can then be summed to find the total energy yield.

2.2.4 SolarSIM

The SolarSIM-G (see figure 2.17) is a measurement tool invented by Spectrafy, Inc. that combines nine narrow-wavelength spectral irradiance measurement channels to reconstruct the global solar spectral irradiance in the 280 - 4000 nm range based on a spectral model [44]. It is capable of resolving the spectrum under both clear and cloudy sky conditions. Its counterpart, the SolarSIM-D2, models direct irradiance from six channels and was validated in [45]. From combined global and direct irradiance measurements, the diffuse spectral irradiance can be calculated.

SolarSIM-D2 performs spectral reconstruction based on a model that calculates aerosol optical depth, precipitable water vapour, and atmospheric total column ozone based on its narrow wavelength measurements. The impact of mixed gas absorption, NO_2 absorption, and Rayleigh scat-

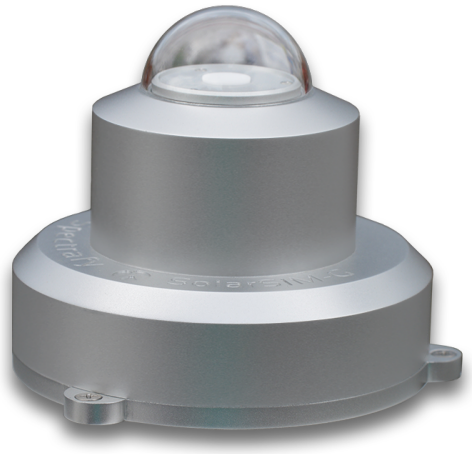

Figure 2.17: Photo of SolarSIM-G device invented and sold by Spectrafy Inc.

tering are determined from temperature and air pressure measurements [46]. The broadband DNI can also be found by integrating the spectral irradiance. The SolarSIM-G has three additional narrow wavelength channels (one in the ultraviolet and two in the infrared range), which help to reconstruct the diffuse irradiance [44].

SolarSIM devices are unique in the PV industry as tools for spectral measurement, providing spectral and atmospheric data in one affordable device. In this work, I drew from National Resources Canada's CanSIM database, which provides global, diffuse, and direct spectral data for various Canadian cities using SolarSIM devices. This volume and range of spectral data is typically difficult and expensive to obtain, and the data provided a unique contribution to this work.

2.2.5 Simulation Procedure

The following diagrams describe the simulation procedure that I followed to obtain the results described in chapters 4 and 5 of this thesis.

Air Mass Modifier Impact Algorithm

The air mass modifier is a correction factor that accounts for spectral shift due to the sun's changing path length through the atmosphere (air mass). For further details, see chapter 4. The impact of the air mass on energy yield predictions was calculated as follows (see figure 2.18):

1. Generate spectra for a range of air masses using the SMARTS software, following the standard ASTM G-173-03 spectrum with the exception of the Rayleigh (air mass) parameter.
2. Calculate the external quantum efficiency (EQE) of the module using SunSolve.
3. Integrate the air mass spectra with the module EQE to find short-circuit current. Integrate the spectra (both air mass and reference) to find total irradiance. Calculate the air mass modifier.

4. Incorporate the air mass modifier with the responsivity of the module in the DUET energy yield model.

5. Calculate the energy yield in DUET with and without the air mass modifier to determine the air mass modifier impact.

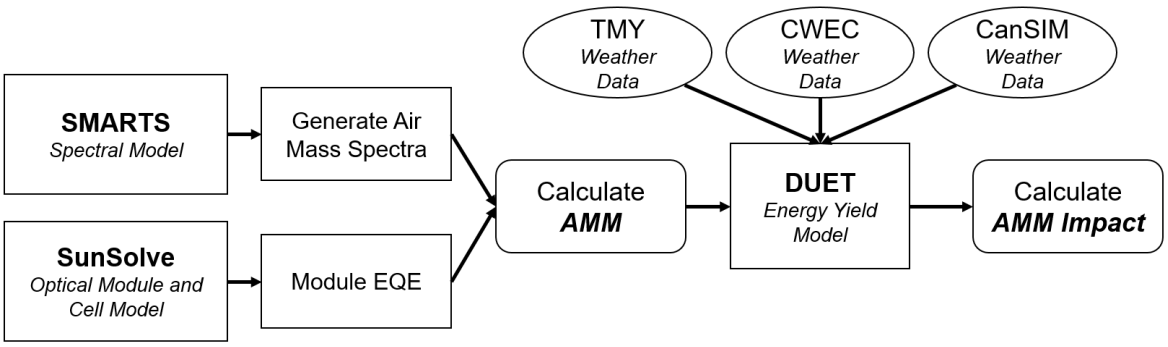

Figure 2.18: Block diagram of the algorithm for calculation of the air mass modifier impact. AMM = air mass modifier. TMY = typical meteorological year. CWEC = Canadian weather year for energy calculation.

Spectral Correction Factor Impact Algorithm

The spectral correction factor is a correction factor for energy yield calculations to account for changing module performance under arbitrary measured spectra. The spectral correction factor is affected by all atmospheric conditions, including air mass, precipitable water content, and ozone (for further details, see chapter 5). It is found by modelling module performance under measured spectra, then adjusting predicted energy yield to account for changing module performance under these spectra. The impact of the spectral correction factor was calculated as follows (refer to figure 2.19):

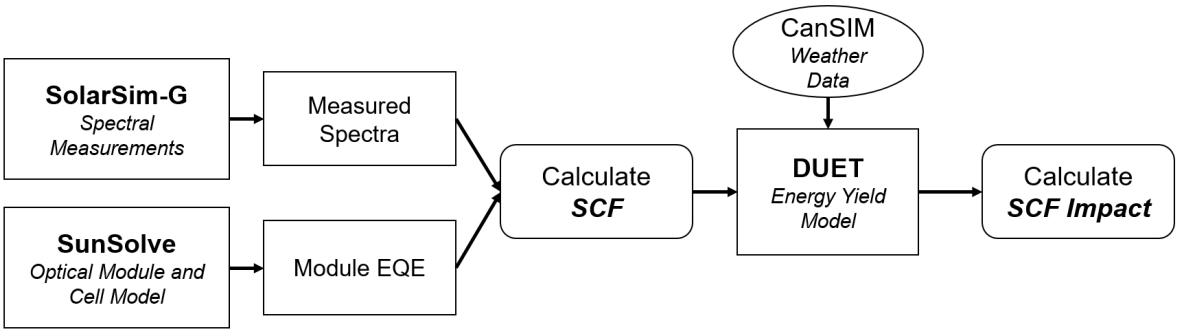

Figure 2.19: Block diagram of the algorithm for calculation of the spectral correction factor impact. SCF = spectral correction factor.

1. Measure spectra for test locations using SolarSIM technology. (Provided to the author by the CanSIM network).

2. Calculate the external quantum efficiency (EQE) of the module using SunSolve.

3. Apply measured spectra to the modeled EQE to find short-circuit current. Integrate the spectra (both measured and reference) to find total irradiance. Calculate the spectral correction factor for each spectrum.

4. Apply the spectral correction factor to module responsivity in DUET.

5. Calculate energy yield in DUET with and without the spectral correction factor to determine the spectral correction factor impact.

2.3 Experimental Methods

2.3.1 External Quantum Efficiency (EQE)

External quantum efficiency (EQE) is the percentage of incident photons that generate an electron-hole pair that are then collected as current (see section 2.1.4). For the quantum efficiency measurements described herein, a Newport IQE-200 quantum efficiency system was used.

To measure quantum efficiency (see figure 2.20), the light from a source passes through the filter wheel, then through an optical chopper, which adds a periodic on-off signal to the light beam. The monochromator selects a narrow wavelength range (~5 nm FWHM), then a beam splitter shines light on the sample and on a reference cell. The reference cell and test sample signals are amplified by preamplifiers, then by the lock-in amplifier. The on-off periodic signal created by the optical chopper and synchronized to the lock-in amplifier allows for a more accurate measurement, since the signal can be filtered at the chopper frequency. The signal is then fed back to the control software where the quantum efficiency is calculated.

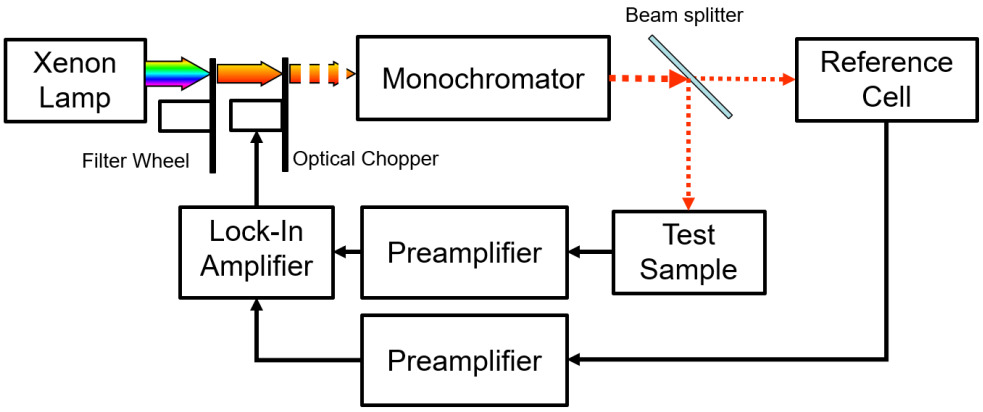

Figure 2.20: Diagram of external quantum efficiency (EQE) test setup.

For quantum efficiency measurements performed at non-normal incidence, the sample under test was mounted on a rotating stage, as shown in figure 2.21. The stage was designed such that the axis of rotation was at the level of the beam's point of incidence on the cell's surface.

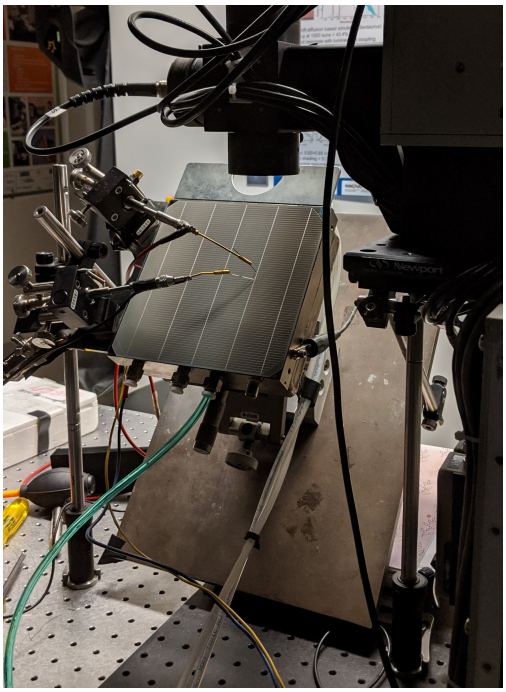

Figure 2.21: Photo of external quantum efficiency (EQE) measurement setup at 40° angle of incidence. Set up in a four-point probe configuration, with two probes contacting the front fingers and two connections to the rear chuck.

2.3.2 Fabrication of Optical Test Samples

In this work, optical test samples were fabricated to measure the complex refractive indices (refractive index, n, and extinction coefficient, k) of silicon heterojunction thin films (ITO and a-Si:H). The samples were fabricated at Arizona State University (ASU) in their class 10,000 clean room facility, the Solar Power Laboratory. This facility provided a constant temperature of 19°C and humidity of 42%.

For silicon substrate samples, 2-inch single-side polished round substrates were cleaned by the following steps: RCA-B solution of 1:1:6, HCl:H_2O_2:H_2O at 75°C for 10 minutes to remove ion impurities; a Pirahna bath of 4:1, H_2SO_4:H_2O_2 at 110°C for 15 minutes to remove organics; and a buffered oxide etch (BOE) of 10:1, H_2O_2:HF at 19°C for 10 minutes as an oxide etch. Each of these steps was followed by a 10-minute DI water bath. The glass slides were cleaned by a 3-step process, 5 minutes each in acetone, isopropyl alcohol, and distilled water in a sonicating bath.

Hydrogenated amorphous silicon (a-Si:H) thin-film layers were deposited on a single side using plasma-enhanced chemical vapour deposition (PECVD) with an Applied Materials P5000 PECVD (see figure 2.22). Since this tool is designed for standard 156 mm square wafers, substrates were placed on carrier wafers. Silane (SiH_4) and hydrogen (H_2) were used for the deposition of intrinsic films, and phosphine (PH_3) and diborane (B_2H_6) were used as dopant gas flows for the n-type and p-type amorphous silicon, respectively. Depositions were performed at 250°C. The resistivity of films deposited with the recipe used were reported to be 18,000 Ω-cm for p-type and 90 Ω-cm for n-type [47].

Indium-tin-oxide (ITO) deposition was performed using an MRC-944 direct-current magnetron

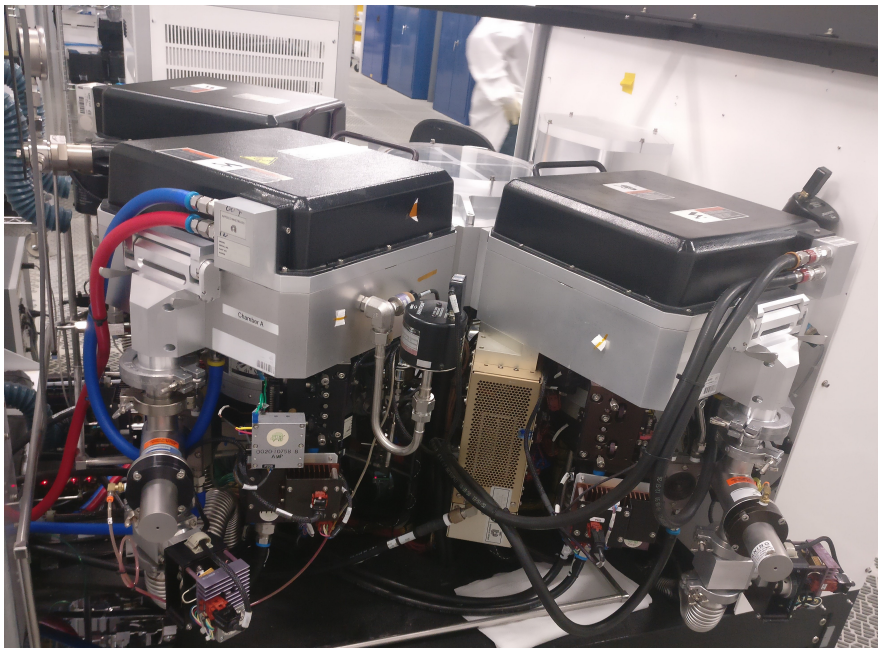

Figure 2.22: Photo of Applied Materials P5000 PECVD at Arizona State University's Solar Power Lab.

sputtering tool at 5.5 mT with 3% oxygen gas concentration and 1kW power. Samples were annealed in a muffle furnace at 280°C for 30 minutes.

2.3.3 Ellipsometry

Ellipsometry is a method of characterizing thin films by measuring the polarization of light that is reflected from a film at a known angle of incidence. The light incident on the film has a known polarization state, and the change of polarization of the reflected light beam is used to evaluate the material's optical and structural properties. The thickness of a thin film, as well as the complex refractive index (n and k), can be determined.

To determine the thin film's properties, the change in the polarization of light, defined by the ellipsometric angles (amplitude ratio, Ψ, and phase difference, Δ), is measured. First, light with a known polarization state is created through a polarizer and compensator, and shines on the sample. Then, the reflected light passes through a polarizer and its ellipsometric angles are measured. A model must then be used to determine the film properties from these measurements.

In this work, ellipsometry was performed using a J.A. Woollam M-2000 ellipsometer with a translation stage (see figure 2.23). The thin films on silicon substrates were measured at 65°, 75°, and 85°, while those with glass substrates were measured at 50°, 55°, and 60°. These angles are near the Brewster angle of the substrates (approximately 74° for silicon and 56° for glass), taking advantage of the larger difference between the parallel and perpendicularly polarized components of the reflected light at this angle. These measurements result in six datasets (two measured properties, three measurement angles) that can be fit, which is more robust than fitting for a single measurement angle. Ellipsometry was performed for a range of wavelengths from 193 - 1690 nm in 1.6 nm increments for wavelengths below 1000 nm and 3.5 nm increments for wavelengths above 1000 nm.

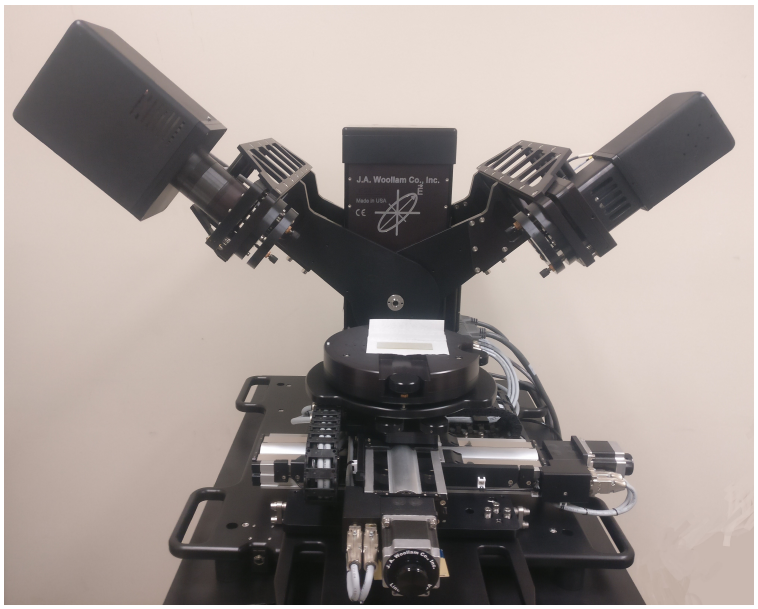

Figure 2.23: Photo of J.A. Woollam M-2000 ellipsometer at Arizona State University's Eyring Materials Center.

Hydrogenated amorphous silicon (a-Si:H) layers were modeled using the Tauc-Lorentz model, and ITO layers were modeled using the Lorentz-Drude model, which are commonly used for ellipsometry measurements of these materials [48] [33]. Ellipsometry measurements are presented in the following paper in Chapter 3.

Chapter 3

Texturing and High-Angle Performance

3.1 Preface

The following chapter presents a Photovoltaics Specialists' Conference (PVSC) proceeding that describes SunSolve simulations of bifacial silicon heterojunction cells at angles of incidence from 0° to 80° and air masses from 1 to 5. Thin film fabrication procedure and ellipsometry results are described.

It should be noted that the agreement between the simulated and measured quantum efficiency in Fig. 5 is much worse than what is demonstrated in chapter 4 (Fig. 2). After this publication, we made improvements, including: new quantum efficiency measurements, the addition of a reflecting layer behind the cell which improved agreement in long-wavelengths, and fine-tuning of modeled thin film layer thicknesses which greatly improved agreement in the UV range.

In this chapter, cell performance with increasing air mass is presented, normalized with respect to incident current (J_{inc}) in the 300 - 1200 nm range. Later, we normalize for the entire spectral range, 280 - 4000 nm, with respect to intensity.

3.2 Co-Author Contributions

M. R. Lewis cleaned thin-film substrates and assisted with thin-film depositions, measured samples via ellipsometry, created the SunSolve model, performed the analysis, and wrote the manuscript.
E. M. Tonita performed EQE measurements and assisted in manuscript revision.
C. E. Valdivia guided methodology and analysis and assisted in manuscript revision.
R-J. K. Obhi assisted with EQE measurements.
J. Leslie performed PECVD depositions for a-Si:H thin film samples.
M. I. Bertoni supervised work performed at ASU, including sample preparation, and provided finished bifacial SHJ cells for EQE measurements.

K. Hinzer oversaw the research and the manuscript.

All authors contributed to the manuscript.

3.3 Publication

The publication is included on the next page. A shortened version of this proceeding was reviewed and accepted by the technical conference committee. The full version was reviewed by conference editors.

M. R. Lewis, E. M. Tonita, C. E. Valdivia, R-J. K. Obhi, J. Leslie, M. I. Bertoni, and K. Hinzer, "Angular Dependence of Textured Bifacial Silicon Heterojunction Solar Cells for High Latitudes," in 2019 IEEE 46th Photovoltaic Specialists Conference (PVSC), 2019, pp. 1919–1923.

Angular Dependence of Textured Bifacial Silicon Heterojunction Solar Cells for High Latitudes

Mandy R. Lewis[1,2], Erin M. Tonita[1], Christopher E. Valdivia[1], Ras-Jeevan K. Obhi[1], Joswin Leslie[2], Mariana I. Bertoni[2], and Karin Hinzer[1]

[1]SUNLAB, Centre for Research in Photonics, University of Ottawa, Ottawa, Ontario, K1N 5N5, Canada
[2]DE*f*ECT Lab, Arizona State University, Tempe, AZ 85281, USA

***Abstract* — Bifacial photovoltaics at high latitudes can achieve up to 25-45% bifacial gain due to high-albedo snow cover and high proportion of diffuse light. We studied the angular performance of bifacial silicon heterojunction solar cells with various textures to understand high-latitude effects on optical losses. For cone and pyramid-patterned designs, external quantum efficiency decreases at high angles, primarily due to increased reflectivity, although longer path length through front-surface films also increases UV losses for all surface types. At 80° incidence and 25°C, a <7% reduction in short-circuit current due to change in external quantum efficiency is observed for random pyramid textured surfaces. Simulation is compared to measured external quantum efficiency for a silicon heterojunction cell, and similar trends are observed with increasing angle of incidence. A relative reduction of <1% in short-circuit current is also observed when moving from an air mass of 1.5 to 5 at high angles of incidence. These results will inform future solar heterojunction designs for this application and be applied to refine annual energy yield calculations.**

***Index Terms* — air mass, angle of incidence, amorphous silicon, bifacial photovoltaics, heterojunction cell, indium-tin-oxide, photovoltaic cells, ray tracing, silicon solar cell, texture.**

I. Introduction

Many northern and remote communities rely on diesel energy, but this use of fossil fuel is expensive and has a disproportionate high impact on fragile environments. Bifacial photovoltaics, or photovoltaic cells that absorb light from the rear in addition to the front, present a clean and low cost alternative.

Bifacial solar energy yield increases with high albedo, high proportion of diffuse light, and low temperature, conditions which are common in Arctic locations. These operating conditions also diverge from standard test conditions of 0º angle of incidence, 25ºC, and AM1.5, namely due to high air mass, low temperature, and high angle of incidence.

For example, the Arctic community of Cambridge Bay, Nunavut, located at 69.1°N, has an average global horizontal irradiance (GHI)-weighted air mass of >3.1 and the proportion of diffuse horizontal irradiance (DHI) to GHI is 44.5%. In this location, the average direct normal irradiance (DNI)-weighted angle of incidence on the rear side of a latitude-tilt bifacial panel is very high at 77°. Energy yield projections for modules at high latitudes would be improved if cell performance under these conditions is taken into account.

Silicon heterojunction (SHJ) solar cells currently hold the record for silicon solar cell efficiency, at 26.7% [1], and are easily adaptable to bifacial applications [2]. However, these cells are typically designed and characterized for regions approximating AM1.5G operating conditions. More precise energy yield analysis of bifacial cells and panels for these conditions will reduce investment risk, resulting in a faster shift towards deployment of bifacial technologies.

II. Characterization of Thin Films

The optical properties of hydrogenated amorphous silicon (a-Si:H) and indium-tin-oxide (ITO) thin films depend strongly on their deposition parameters; these include substrate temperature, film thickness, and substrate material. Therefore, it is important to input experimental values in simulation models in order to get accurate predictions.

In this case, we seek to characterize annealed and as-deposited ITO films and PECVD-deposited doped and intrinsic a-Si:H layers across the range of parameters to be used in the modeling of heterojunction cells. A range of deposition thicknesses was tested in order to better optimize layer parameters.

A. Fabrication

Layers of a-Si:H were deposited on crystalline silicon (c-Si) substrates. Substrates were cleaned for 10 minutes in RCA-B (6:1:1 H_2O:H_2O_2:HCl) at 75°C (ionic clean) and 10 minutes in Pirahna (8:1 H_2O:H_2SO_4) at 110°C (organic clean). Just before deposition, the samples were dipped in buffered oxide etch (BOE) at room temperature to remove the native oxide layer.

Varying thicknesses of a-Si:H were then deposited using an Applied Materials P5000 PECVD at a frequency of 13.6 MHz and a substrate temperature of 250°C. Silane (SiH_4) and hydrogen (H_2) were used for the deposition of intrinsic films, and phosphine (PH_3) and diborane (B_2H_6) were used as dopant gas flows for the n-type and p-type amorphous silicon, respectively. The resistivity of films deposited with the recipe used were reported to be 18,000 Ω-cm for p-type and 90 Ω-cm for n-type [3].

Varying thicknesses of ITO were deposited on glass substrates. Substrates were cleaned by 5-minute sonication in acetone, isopropyl alcohol, and distilled water. ITO was then deposited by sputtering at 1 kW power with 3% O_2 flow at 5.5 mT.

B. Ellipsometry

For the a-Si:H samples, ellipsometry measurements were taken using a J.A. Woollam M-2000 ellipsometer with incidence angles of 65°, 75°, and 85°. To obtain optical constants, we applied the Tauc-Lorentz model, the commonly accepted method to simulate a-Si:H [4]. Results are shown in Figure 1.

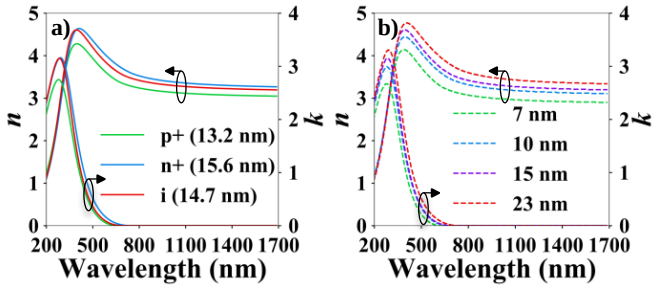

Fig.1. Optical constants for a-Si:H layers of (a) varied doping and (b) varied thickness, deposited on c-Si substrates, measured by ellipsometry.

The optical constants of p-type a-Si:H, shown in figure 1a, are lower than intrinsic due to the increased boron doping level, as expected [5], [6]. The measurements follow trends from previous studies; while the n-type and intrinsic curves may be affected by their difference in thickness, phosphorous doping has also been associated with reduced bandgap and increased refractive index [7].

Figure 1b shows that optical constants increase with thickness. The trend of higher bandgap and reduced refractive index for thinner films of a-Si:H has two possible explanations: (1) higher hydrogen content and presence of nano-clusters in the interface region between the a-Si and c-Si [4], and (2) quantum effects [8]. This trend was also observed for n-type a-Si:H, although the trend in p-type films was not clear.

For the ITO samples, ellipsometry was performed with incidence angles of 50°, 55°, and 60°, and we applied the Lorentz-Drude model for analysis. Measurements were taken after deposition, then again after annealing at 280°C for 30 minutes. Figure 2 shows that the absorption in the ITO increases after annealing, as expected [9].

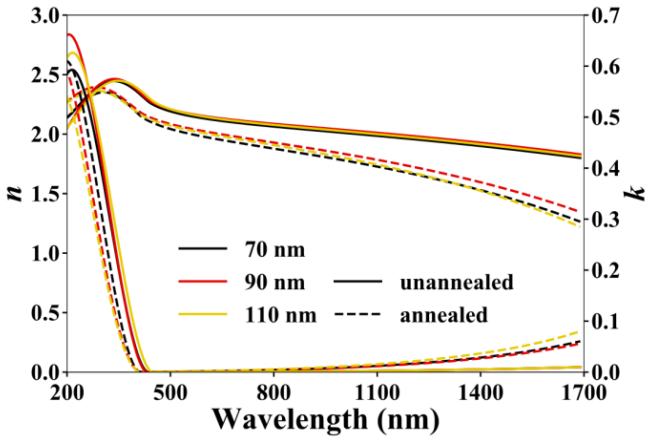

Fig. 2. Optical constants for ITO layers of varied thickness, deposited on glass, before and after annealing.

III. Quantum Efficiency at High Incident Angle

To determine the optical behavior of solar cell designs, simulations were performed using SunSolve™, a Monte Carlo ray-tracing online software from PV Lighthouse that evaluates thin-film and surface texturing optical effects. Figure 3 depicts the bifacial SHJ layer structure used in this work. Ellipsometry results for a-Si:H and ITO layers were used as model inputs.

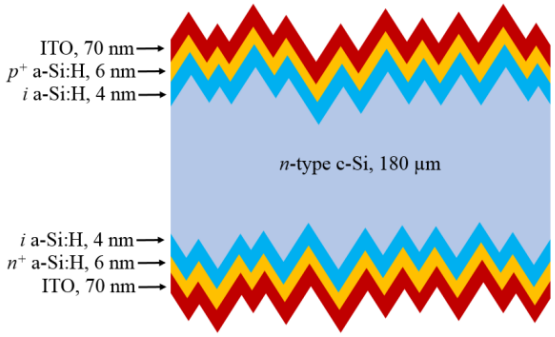

Fig. 3. Schematic of the simulated bifacial silicon heterojunction solar cell layer structure with random pyramidal surface texturing on both faces.

Four surface morphologies were studied: planar, random upright cones, periodic inverted pyramids, and random upright pyramids. The effect of angle of incidence on external quantum efficiency (EQE) was simulated for each surface texture, including shading losses from fingers and busbars. Simulations were run with a total of 5×10^6 rays and for 10-nm wavelength steps over the absorption range of c-Si. Figure 4 shows the EQE and 1 - reflectivity of these structures as angle of incidence increases from 0° to 80°.

As expected, reflectivity increases across the spectrum with increasing angle for all textures. The planar solar cell (Fig. 4a) has the highest reflectivity over all angles, particularly in the ultraviolet (UV) and near infrared (IR). We also observe that the reflectivity minimum shifts to smaller wavelengths as the angle of incidence increases, as previously observed by Geisemeyer *et al.* [10]. The addition of surface texturing reduces the overall reflectivity for all angles of incidence at all wavelengths.

Although inverted pyramids had approximately 0.5% higher average reflectivity than upright pyramids for 50º to 80º angle of incidence, the result was otherwise similar. Some sources have found that regular inverted pyramids result in a higher internal quantum efficiency (IQE) due to reduced density of surface defects and therefore lower surface recombination velocity [11]. This effect is not captured in these SunSolve simulations since electrical properties of the cells are not included in the modeling package.

Note that EQE for all textures is reduced in the low wavelength range due to parasitic absorption in the front surface layers. A further reduction in EQE could be observed due to front surface recombination because carriers generated by short-wavelength light are absorbed near the cell surface; however, this effect is not captured in the SunSolve model. The high wavelength range, by comparison, has reduced EQE due to low absorption in c-Si at long wavelengths, resulting in

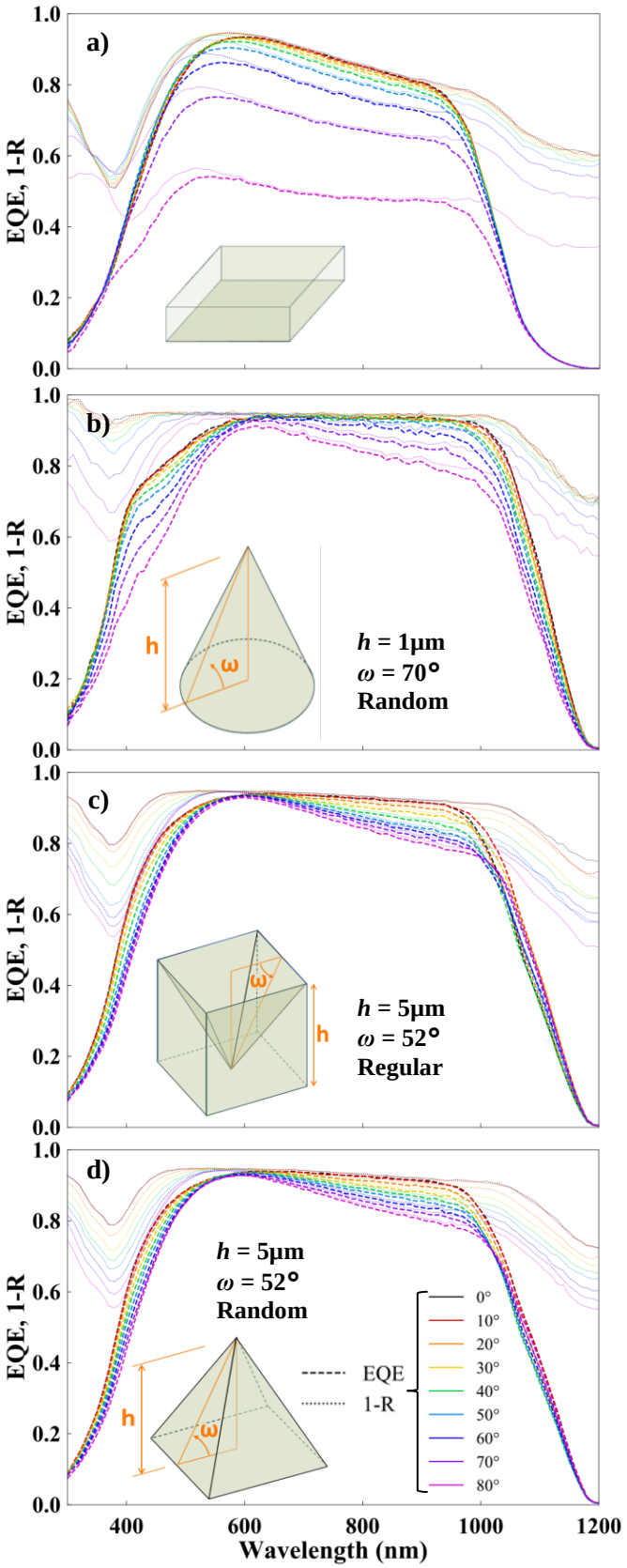

Fig. 4. External quantum efficiency (heavy dashed lines) and 1 - reflection (light dashed lines) for a solar cell with a) planar, b) 70° random 1-µm tall cones, c) 52° 5-µm tall regular inverted pyramids, d) 52° 5-µm tall random upright pyramids for angles of incidence from 10° to 80°.

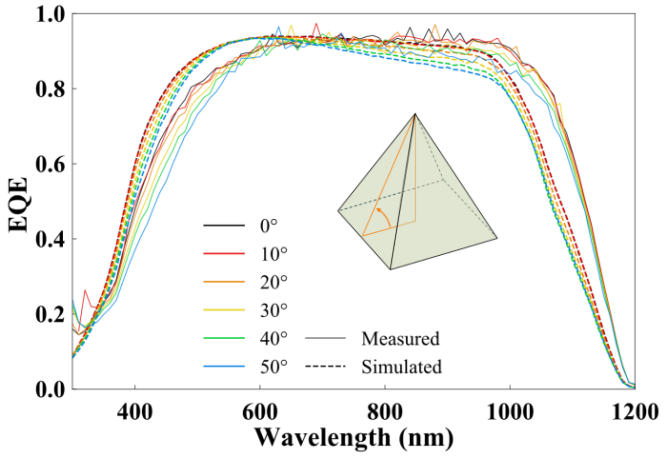

Fig. 5. Measured and simulated EQE for a random upright pyramidally textured solar heterojunction cell for angles of incidence from 10° to 50°.

higher cell transmission and front surface escape. EQE is also reduced at all wavelengths by reflected light.

The cone-textured cell (Fig. 4b) demonstrates a larger reduction in the EQE with increasing angle compared to the inverted or upright pyramidally textured cells. This is due to high parasitic absorption in the front a-Si:H layers, from 3.0% at 0º angle of incidence to 4.3% at 80º, and increased reflectivity, from 5.4% at 0º to 15.6% at 80º. The a-Si:H layer absorption, in particular, causes a greater impact in the <600 nm EQE range compared to pyramidal cells.

Figure 5 includes the measured EQE performance of a bifacial silicon heterojunction solar cell with random upright pyramidal texturing on both faces. The cell was measured on a stage with adjustable tilt of up to 50° angle of incidence. A xenon arc lamp coupled with a monochromator was used to scan through the wavelength range of interest. Measured values were then adjusted to account for anticipated shading losses of the fingers and busbars.

As in the simulated EQE, the measured EQE is reduced under high angles of incidence, especially in the ultraviolet (UV) (<400 nm) and infrared (IR) (>1000 nm). However, the measured solar cell exhibits greater absorption in the IR than in simulation due to the reflective chuck placed beneath the cell during EQE measurements, resulting in a 1 mA/cm^2 increase in J_{SC}. The measured EQE is smaller than the simulated EQE in the UV range for all angles, possibly due to high surface recombination of carriers generated by short-wavelength light at the front of the cell.

Figure 6 shows the modeled optical losses at 0° and 80° for the structure defined in figure 3 with a random pyramidal surface. J_{SC} is reduced from 37.5 mA/cm^2 at 0° to 6.1 mA/cm^2 at 80°. This reduction in short-circuit current is primarily due to cosine losses, which cause an 82.6% reduction in incident power. Cell absorption, comparatively, is only reduced from 81.1% at 0° to 75.4% at 80°.

The reduction in EQE with increasing angle is primarily due to the increase in reflectivity at the air-ITO interface from 7.5% to 16.1%. Reflected loss also includes the effects of shading due

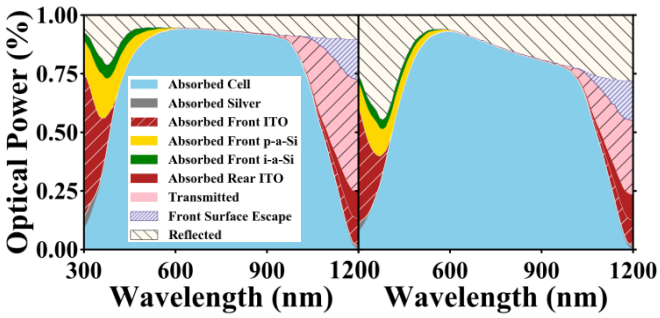

Fig. 6. Modeled sources of optical loss in upright pyramidal bifacial silicon heterojunction solar cell at a) 0° and b) 80° under AM1.5G spectrum.

to fingers and busbars. In the UV range, parasitic absorption in the front a-Si:H layers and ITO cause the most optical loss (40.6% of UV light at 0º, or 0.6 mA/cm^2), while absorption in both ITO layers causes loss in the IR (7.8% of IR light at 0º, or 0.7 mA/cm^2). Escaped light is also a significant source of loss in the IR, with 28.3% escape from the rear (2.5 mA/cm^2) and 5.6% escape from the front (0.5 mA/cm^2).

While in practice, carrier collection can occur due to absorption in the a-Si films, SunSolve considers all absorption in amorphous silicon to be parasitic. In reality, the short diffusion length of carriers in a-Si results in a low collection probability. In our model, the highest EQE is obtained with the thinnest possible amorphous silicon layers, since this reduces parasitic absorption. However, with layer thickness there is a tradeoff between optical losses and passivation quality of the silicon interface. For example, it has been shown that surface recombination velocities decrease dramatically to below 1 cm/s as a-Si:H layer thickness increases from 10 nm to 50 nm [12].

To simulate high air mass conditions, input spectra for varying air mass were generated by SMARTS simulation and applied to the SunSolve model of a pyramidal cell. Total irradiance is reduced at high air mass, resulting in a 51% relative reduction in J_{sc} from AM1.5G to AM5.0G for all angles of incidence, as shown in figure 7.

In addition, for all air masses, J_{sc} was reduced by 83.8% from 0° to 80° angle of incidence. This was primarily due to cosine loses, which caused an 82.6% reduction in incident power from 0° to 80° for all air masses. Changing EQE with respect to angle resulted in the remaining 1.2% reduction in J_{sc}.

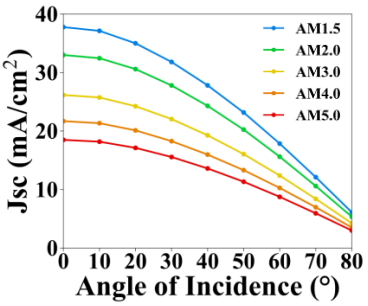

Fig. 7. Modeled random pyramidal bifacial silicon heterojunction solar cell short-circuit current density as a function of incidence angle under spectra of varying air mass.

J_{sc} was apparently insensitive to changes in the input spectrum, with less than 1% difference between J_{sc} for all angles of incidence between AM1.5G and AM5.0G when normalized for differences in intensity.

IV. Summary

The performance of planar and textured bifacial silicon heterojunction solar cells has been studied for angles of incidence up to 50-80°. Reflectivity had the highest impact on EQE with changing angle, highlighting the best anti-reflection treatments for a wide range of angles for northern deployments.

This optimization of bifacial SHJ solar cells for high-latitude operating conditions will aid in the fabrication of bifacial solar panels enhanced for high-latitude deployment.

Acknowledgement

The authors would like to thank William Weigand and Zhengshan Yu for their assistance with sample fabrication at Arizona State University's Solar Power Lab. We acknowledge the support of the Natural Sciences and Engineering Research Council of Canada (NSERC), [NSERC CREATE 497981 and NSERC STPGP 521894].

Experimental work was partially supported by the Engineering Research Center Program of the National Science Foundation and the Office of Energy Efficiency and Renewable Energy of the Department of Energy under NSF Cooperative Agreement No. EEC-1041895. Any opinions, findings and conclusions or recommendations expressed in this material are those of the author(s) and do not necessarily reflect those of the National Science Foundation or Department of Energy.

References

[1] K. Yamamoto, K. Yoshikawa, H. Uzu, and D. Adachi, "High-Efficiency Heterojunction Crystalline Si Solar Cells," *Jpn. J. Appl. Phys.*, vol. 57, no. 8S3, p. 08RB20, 2018.

[2] J. Libal and R. Kopecek, Eds., *Bifacial Photovoltaics: Technology, applications and economics*. London, UK: The Institution of Engineering and Technology, 2018.

[3] S. Y. Herasimenka, "Large Area Ultrapassivated Silicon Solar Cells Using Heterojunction Carrier Collectors," Arizona State University, 2013. (Thesis).

[4] Y. Abdulraheem, I. Gordon, T. Bearda, H. Meddeb, and J. Poortmans, "Optical bandgap of ultra-thin amorphous silicon films deposited on crystalline silicon by PECVD," *AIP Adv.*, vol. 4, no. 5, 2014.

[5] Z. C. Holman *et al.*, "Current losses at the front of silicon heterojunction solar cells," *IEEE J. Photovoltaics*, vol. 2, no. 1, pp. 7–15, 2012.

[6] K. Yoon *et al.*, "Preparation and characterization of p-type hydrogenated amorphous silicon oxide film and its application to solar cell," *J. Non. Cryst. Solids*, vol. 357, no. 15, pp. 2826–2832, 2011.

[7] G. Srinivasan and A. S. Nigavekar, "Role of dopants in the electronic structure of hydrogenated amorphous silicon," *Mater. Sci. Eng. B*, vol. 8, no. 1, pp. 23–37, 1991.

[8] J. Müllerová, L. Prušáková, M. Netrvalová, V. Vavruňková,

and P. Šutta, “A study of optical absorption in amorphous hydrogenated silicon thin films of varied thickness,” *Appl. Surf. Sci.*, vol. 256, no. 18, pp. 5667–5671, 2010.

[9] N. M. Khusayfan, “Study of Structure and Electro-Optical Characteristics of Indium Tin Oxide Thin Films,” vol. 2013, 2013.

[10] I. Geisemeyer *et al.*, “Angle Dependence of Solar Cells and Modules: The Role of Cell Texturization,” *IEEE J. Photovoltaics*, vol. 7, no. 1, pp. 19–24, 2017.

[11] H. P. Wang, A. C. Li, T. Y. Lin, and J. H. He, “Concurrent improvement in optical and electrical characteristics by using inverted pyramidal array structures toward efficient Si heterojunction solar cells,” *Nano Energy*, vol. 23, pp. 1–6, 2016.

[12] S. Shanmuga Priya, A. Rao, I. Thirunavukkarasu, and V. Nayak, “Solar pebble bed reactor for treatment of textile and petrochemical industrial wastewater,” *Int. J. ChemTech Res.*, vol. 9, no. 11, pp. 261–270, 2016.

Chapter 4

Impact of Air Mass on Energy Yield in High-Latitude Locations

4.1 Preface

In this chapter, we model encapsulated modules rather than bare cells (with the exception of model validation in section II.B). The optical constants used in the model for the glass, EVA, and c-Si layers are presented in figure 4.1. These were taken from the built-in SunSolve refractive index library by PV Lighthouse, which refer to various sources [49][50][51][52].

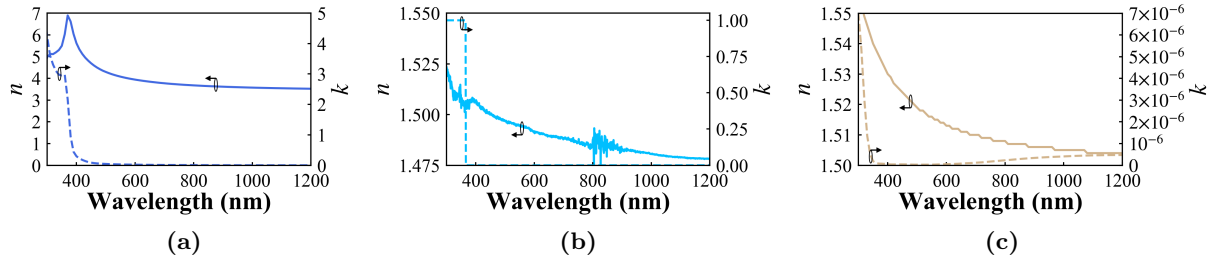

Figure 4.1: Optical constants of a) crystalline silicon, b) ethylene vinyl acetate, and c) glass used in module model. Retrieved from PV Lighthouse refractive index library [49][50][51][52].

The optical losses in the cell with respect to wavelength at 0° and 80° angle of incidence are shown in figure 4.2. The bare cell demonstrates a high level of parasitic absorption in the short wavelength range due to absorption in the front surface layers (a-Si:H and ITO), as discussed in Chapter 3. The module has increased short-wavelength parasitic absorption in this range due to additional parasitic absorption in the EVA and glass. For both the bare and encapsulated cell, reflectivity is the greatest source of increased loss between 0° and 80° angle of incidence. Performance with respect to angle of incidence changes dramatically when the cell is encapsulated, primarily due to the glass-air interface, which dominates the reflectivity characteristics of the module.

In this chapter, the external quantum efficiency of a bare cell modeled in SunSolve is compared to the measured quantum efficiency of a silicon heterojunction cell fabricated at ASU. A layer of nickel was added to the SunSolve model to simulate the reflective chuck that sat beneath the cell

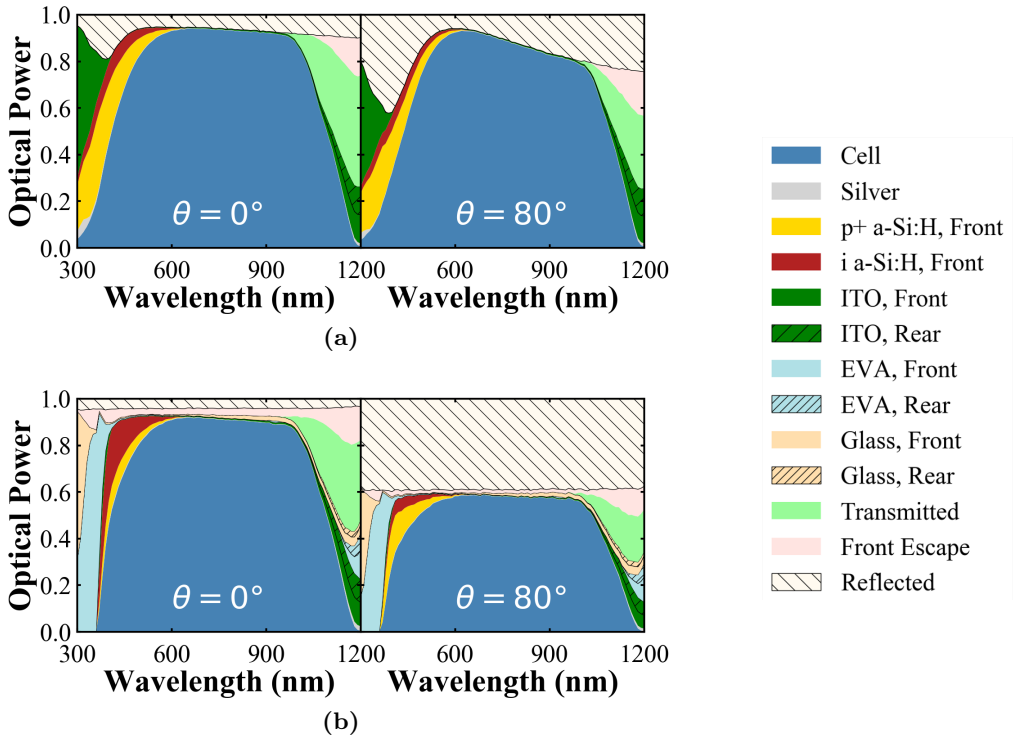

Figure 4.2: Optical losses in silicon heterojunction a) cell and b) module at 0°and 80°angle of incidence.

during the quantum efficiency measurements. The measured quantum efficiency was reduced by the expected shading losses in the silver contacts over the entire cell (a shading factor of approximately 6%). The nickel layer was then removed from the model for the optical loss, incidence angle, and air mass calculations shown in Fig. 3, 4, and 5.

The following chapter describes the air mass modifier, how it is calculated, and its impact on energy yield predictions. The impact of air mass on energy yield is demonstrated and air mass correction is shown to be more significant with increasing latitude.

4.2 Co-Author Contributions

M. R. Lewis created the SunSolve model, measured cell EQE, performed DUET simulations, performed the analysis, and wrote the manuscript.
A. C. J. Russell co-wrote the DUET software, incorporated the AMM in DUET, performed preliminary DUET simulations, wrote the first draft of section III, and assisted in manuscript revision.
C. E. Valdivia co-wrote the DUET software, guided methodology and analysis, and assisted in manuscript revision.
J. E. Haysom supervised and advised A.C.J. Russell.
M. I. Bertoni supervised work performed at ASU, including sample preparation, and provided finished bifacial SHJ cells for EQE measurements.
K. Hinzer oversaw the research and the manuscript writing.

All authors contributed to parts of the manuscript.

4.3 Publication

The publication is included on the next page. A shortened version of this proceeding was reviewed and accepted by the technical conference committee. The full version was reviewed by conference editors.

M. R. Lewis, A. C. J. Russell, C. E. Valdivia, J. E. Haysom, M. I. Bertoni, and K. Hinzer, "Impact of Air Mass on Energy Yield Calculation for Bifacial Silicon Heterojunction Photovoltaic Modules in High-Latitude Conditions," in 2020 IEEE 47th Photovoltaic Specialists Conference (PVSC), 2020.

Impact of Air Mass on Energy Yield Calculation for Bifacial Silicon Heterojunction Photovoltaic Modules in High-Latitude Conditions

Mandy R. Lewis
SUNLAB
University of Ottawa
Ottawa, ON
DEfECT Lab
Arizona State University
Tempe, AZ

Annie C. J. Russell
SUNLAB
University of Ottawa
Ottawa, ON

Christopher E. Valdivia
SUNLAB
University of Ottawa
Ottawa, ON

Joan E. Haysom
J. L. Richards & Associates Ltd.
Ottawa, ON
SUNLAB,
University of Ottawa
Ottawa, ON

Mariana I. Bertoni
DEfECT Lab
Arizona State University
Tempe, AZ

Karin Hinzer
SUNLAB
University of Ottawa
Ottawa, ON

***Abstract*—At high latitudes, bifacial photovoltaics are expected to achieve significant bifacial gain due to the albedo of snow, but irradiance will include a wide range of incident angles and high air mass spectra. We studied the performance of bifacial silicon heterojunction solar modules with increasing angle of incidence and air mass to derive an incidence angle modifier and air mass modifier for short circuit current. We found that the incidence angle modifier remained constant with varied air mass, allowing the incidence angle modifier and air mass modifier to be applied independently. Module correction factors were applied to the SUNLAB's energy yield model, DUET. We demonstrate that the impact of air mass on energy yield increases with latitude and can reach >2.5% on an annual basis for single-axis tracked modules and >2% for fixed latitude-tilt modules in high-latitude locations. This is highly dependent on season, with greater impact in off-summer months, reaching >6.5% monthly air mass impact for a high-latitude location in winter. These results demonstrate that air mass effects are more significant for high-latitude locations, and should be considered in energy yield calculations.**

Keywords— air mass, angle of incidence, bifacial photovoltaics, energy yield model, heterojunction cell, photovoltaic cells, ray tracing, silicon solar module.

I. Introduction

Many northern and remote communities rely on expensive diesel fuel that has a disproportionately high impact on sensitive environments. Bifacial photovoltaics, or photovoltaic (PV) cells that absorb light from the front and rear sides, present a clean and low-cost alternative. Silicon heterojunction (SHJ) solar cells currently hold the record for silicon solar cell efficiency, at 26.7% [1], and are easily adaptable to bifacial applications. However, these cells are typically characterized for standard test conditions of AM1.5, 25ºC, and 0º angle of incidence (AOI, the angle measured from normal incidence).

Due to high air mass (AM), low temperature, high AOI, and variable albedo, high-latitude operating conditions diverge substantially from standard test conditions. Air mass (the ratio of the sun's path length through the atmosphere to the thickness of the atmosphere) reduces spectral UV content as it increases and is higher in high-latitude conditions due high solar zenith angles. Table I shows average meteorological conditions calculated from Canadian Weather Year for Energy Calculation (CWEC) and Typical Meteorological Year (TMY) datasets. Accurate energy yield predictions for high latitudes require an understanding of solar cell and module performance under these conditions.

For example, an incidence angle modifier (IAM) is typically included in energy yield models, and can be determined experimentally [2] or analytically [3]. In this paper, we calculate the incidence angle modifier for a SHJ module and incorporate it in our energy yield model.

By contrast, spectral effects are often considered negligible in silicon modules; however, this analysis is typically performed for low-latitude locations (e.g. [4],[5]). Air mass, in particular, is rarely accounted for in most silicon PV energy yield models, despite the significant impact that it can have on performance [6]. This paper demonstrates that air mass has a non-negligible impact on energy yield in high-latitude locations, even for silicon.

Accurate energy yield models for high-latitude bifacial panels will reduce investment risk, resulting in a faster shift towards deployment of bifacial technologies. This paper

TABLE I. Average Meteorological Conditions Calculated from CWEC and TMY Datasets

	Phoenix, Arizona	**Ottawa, Ontario**	**Cambridge Bay, Nunavut**
Latitude	33.5°N	45.4°N	69.1°N
Avg. Temp.[a]	29.7°C	13.9°C	-12.9°C
Avg. Air Mass[a]	AM1.8	AM2.2	AM3.1
Snow Cover	0% 0 months	32% 4 months	70% 9.5 months

[a] GHI-weighted average.

We acknowledge the support of the Natural Sciences and Engineering Research Council of Canada (NSERC), [NSERC CREATE 497981 and NSERC STPGP 521894].

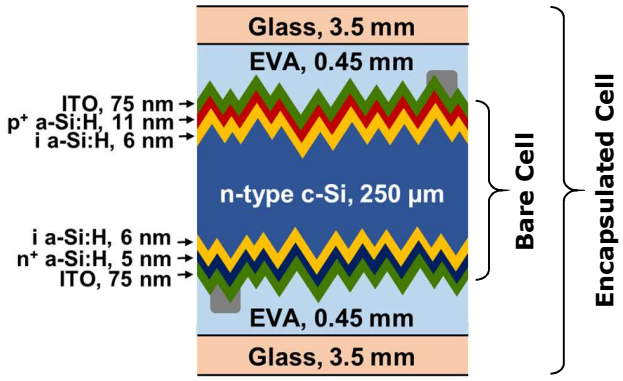

Fig. 1. Schematic of the simulated bifacial SHJ module layer structure. c-Si: crystalline silicon, EVA: ethylene vinyl acetate, a-Si:H: hydrogenated amorphous silicon, ITO: indium tin oxide.

quantifies the impact of air mass on SHJ cell absorption with an air mass modifier. This modifier is applied to incident irradiance in DUET, the SUNLAB's bifacial energy yield model [7], to determine its impact on energy yield for fixed-tilt and tracked systems in Arizona, Ontario, and Nunavut.

II. Module Model and Results

A. Optical Model of Cell and Module

Simulations of the solar cell and module optical behavior were performed using SunSolve, a Monte Carlo ray-tracing online software from PV Lighthouse that can evaluate the optical performance of solar cells and modules, including thin-film effects and surface texturing [8]. Fig. 1 depicts the bifacial SHJ module layer structure used in our model, based on the layer structure described in [9], adapted for bifacial applications. The model includes ellipsometry data for thin-film layers, which include the indium-tin-oxide (ITO) and hydrogenated amorphous silicon (a-Si:H) layers, described in [10]. For bare cell simulations, we remove the encapsulant layers (ethylene vinyl acetate (EVA) and glass) and keep the identical cell structure. Simulations were run in 10-nm steps over the wavelength range of 300-1200 nm with a total of 5×10^6 rays, for light incident on both front and rear faces.

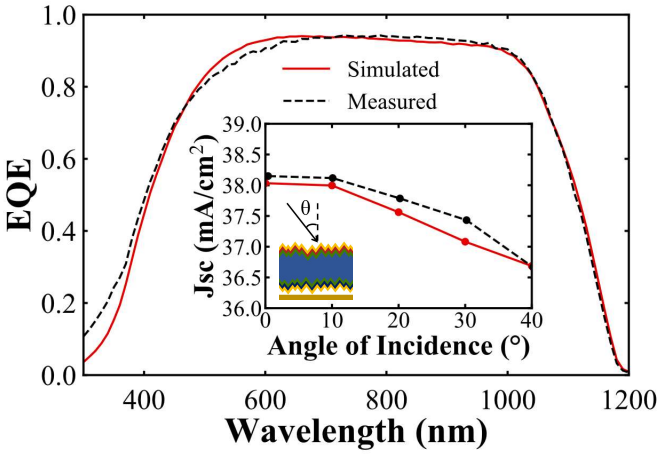

Fig. 2. Measured (black dashed lines) and simulated (red solid lines) external quantum efficiency (EQE) for an unencapsulated silicon heterojunction cell at 0° angle of incidence. Inset: Short-circuit current density (J_{sc}) vs. angle of incidence for unencapsulated silicon heterojunction cell for incidence angles from 0° to 40° under AM1.5G illumination.

B. Validation of Cell Model

We measured the external quantum efficiency (EQE) of a bare silicon heterojunction cell on a reflective metal platform with adjustable tilt of up to 40° AOI. A xenon arc lamp coupled with a monochromator was used to scan through the wavelength range of 300-1200 nm. Measured values were then adjusted to account for shading losses in the cell. To compare measured and simulated EQE (shown in Fig. 2), a reflective layer of nickel was added below the rear face of the cell in the model, which was essential for agreement of long-wavelengths.

The short-circuit current density (J_{sc}) was obtained by integrating the measured and simulated EQE with the standard AM1.5G spectrum. The inset in Fig. 2 shows J_{sc} as a function of angle from 0° to 40° AOI, where 0° is normal to the panel. The difference in J_{sc} is less than ~1.2% for all angles of incidence, and within the uncertainty of the measurement.

C. Module Model Results

1) Module Optical Losses

Fig. 3. displays the simulated module optical losses and cell absorption with respect to wavelength as a percentage of total incident irradiance at 0° and 80° AOI for light incident on the module front face. The cell absorption (in blue) represents the modeled EQE of the module.

Parasitic absorption losses are high for short-wavelength incident irradiance, primarily due to absorption in the front surface layers such as the glass, EVA, and front-surface thin films. Escape losses (which include both transmission and front surface escape) are higher for long-wavelength irradiance due to its lower absorptivity in c-Si.

If reflectivity (R) is ignored, the module EQE, parasitic absorption, and light escape are nearly identical for all angles of incidence. If module EQE at both AOI (0º and 80º) are divided by 1-R, they are less than 4% different for all wavelengths. At high AOI, EQE is increased in the long wavelengths due to longer path lengths through the cell, while it is reduced in the UV due to increased optical path lengths through parasitically absorbing layers. The effect of reflectivity far outweighs these differences with respect to angle, however.

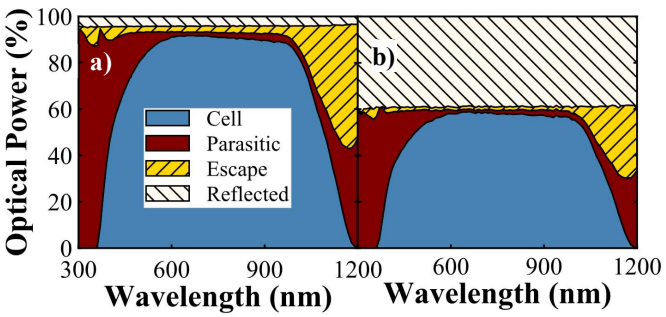

Fig. 3. Modeled sources of optical loss as a percentage of incident irradiance for an encapsulated silicon heterojunction cell under AM1.5G spectrum at (a) 0º and (b) 80º angles of incidence.

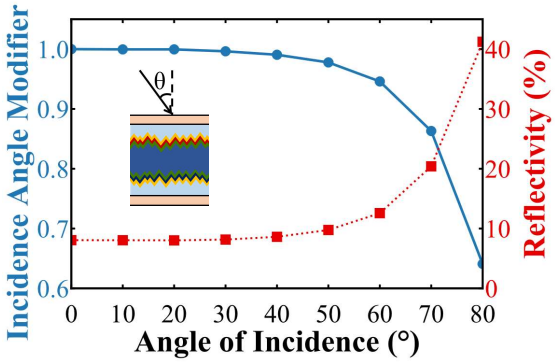

Fig. 4. Simulated incidence angle modifier (blue solid line) and reflectivity (red dashed line) for the module in Fig. 1 for angles of incidence from 0° to 80°.

2) Incidence Angle Modifier

The incidence angle modifier (IAM) improves energy yield calculation accuracy by de-rating the current contribution of high angle of incidence light to account for increased reflectivity and other losses in the module. We define the IAM using the following equation:

$$\mathrm{IAM}(\theta) = \frac{J_{sc}(\theta)}{J_{sc}(0°)} \tag{1}$$

where $J_{sc}(\theta)$ is the short-circuit current density of the module at an angle of incidence, θ, and $J_{sc}(0°)$ is the short-circuit current density at normal incidence.

Module short-circuit current was calculated using our SunSolve model under AM1.5G illumination with varied angles of incidence, ignoring cosine losses. Cosine losses are accounted for separately in the DUET software and are strictly a geometrical factor. Fig. 4 shows the incidence angle modifier and module reflectivity with respect to AOI. As expected, the IAM – and by extension J_{sc} – decreases with increasing AOI. While other factors (such as parasitic absorption) change with AOI, the reflectivity is the dominant effect; from 0° to 80° AOI, there is a 36% relative reduction in J_{sc} and a 35% increase in reflectivity.

The reflectivity follows closely with the unpolarized Fresnel reflection curve for effective refractive indices of 1 for air and 1.5 for glass. For incidence angles higher than the Brewster angle of the glass-to-air interface (approximately 56°), a large increase in reflection results in a sharp reduction in J_{sc} and the IAM.

Comparing incidence angle modifiers for a wide range of air masses shows that they are approximately equal for all air masses studied (1.0 to 38.2), within ~0.1% absolute on average. Therefore, the energy yield calculations below apply the IAM extracted for AM1.5G.

3) Air Mass Modifier

The air mass modifier (AMM) corrects module responsivity, in units of A/W, with respect to air mass to account for changing spectral shape. Each module design has a unique response to changing incident spectra, and consequently has a unique AMM [11].

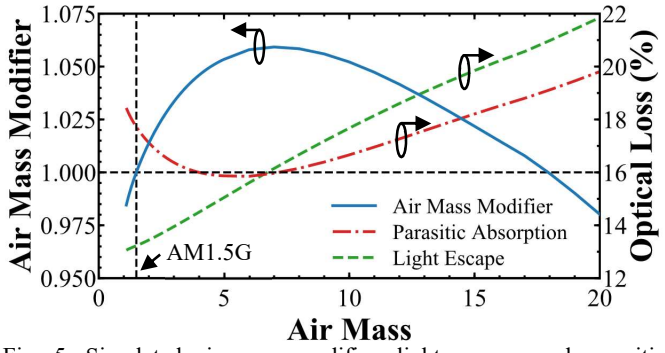

Fig. 5. Simulated air mass modifier, light escape, and parasitic absorption for Fig. 1 module design under AM1.1 to AM20 illumination. Optical losses shown as percentage of incident irradiance.

To simulate high air mass conditions, input spectra for varying air masses were generated in SMARTS and applied to our SunSolve model at 0° AOI. These spectra followed the ASTM AM1.5G standard, varying only the relative air mass parameter. To isolate the impact of spectral shift, the total incident irradiance was normalized to 1000 W/m^2. The air mass modifier (AMM) is defined as:

$$\mathrm{AMM} = \frac{J_{scAMX}}{J_{scref}} \times \frac{Irr_{ref}}{Irr_{AMX}} \tag{2}$$

where J_{scAMX} is the short-circuit current density under a test spectrum with air mass X, J_{scref} is the short-circuit current density under the reference spectrum, Irr_{ref} is the total irradiance of the reference spectrum, and Irr_{AMX} is the total irradiance of the test spectrum. An AMM value larger than one indicates that module power under the given spectrum will be greater than that under the AM1.5G standard spectrum for the same integrated irradiance. The reference spectrum is set at AM1.5, so by definition, the AMM at AM1.5 is equal to one.

The AMM, shown in Fig. 5, follows a similar trend as other types of silicon solar cells at low air masses (AM1-AM5) previously reported (e.g. [12]). For our modeled SHJ cells, AM5-AM10 show the best performance with AMM >1.05, while the AMM remains >1 up to AM18.

Fig. 5 also displays the module parasitic absorption and light escape, as a percentage of incident irradiance, with respect to air mass. Parasitic absorption decreases with increasing air mass because the short-wavelength content of the incident spectrum decreases at high air masses (refer to Fig. 3). Past AM5, parasitic absorption increases due to the increased proportion of incident irradiance that is absorbed parasitically in the long-wavelength range. Light escape increases with rising air mass as the long-wavelength fraction of the incident spectrum increases, further reducing the AMM. In addition, as air mass increases, the spectral irradiance is weighted towards the long wavelengths where spectral responsivity is high.

4) Module Behaviour for Rear-Incident Light

Changes in optical loss with increasing angle of incidence and air mass are nearly identical between the front and rear faces due to the symmetry of the module's design; the only difference between the front and rear layers is the doped a-Si:H

type and thickness. While this affects UV absorption in the doped a:Si:H layer, the effect is small compared to the EVA, glass, and ITO layer absorption. The simulated incidence angle modifiers for the front and rear faces differ by less than 0.1% for all angles, while the air mass modifiers are within 0.5% for all air masses.

The rear-side quantum efficiency is affected by the increased length that carriers generated by rear-incident light must transport to be collected at the pn junction, as shown by measurements and simulations previously performed by our group [13]. Therefore, rear-side IAM and AMM may differ from what is presented here. In the future, the impact of separate modifiers for the front and rear faces will be explored.

III. Energy Yield Model and Results

The IAM and AMM calculated above were integrated into DUET, the SUNLAB's bifacial PV energy yield model for fixed-tilt and tracked systems.

A. Model

DUET is a 3D sectioned view factor model that accounts for mounting structure shading. The software divides a diffuse sky dome, reflecting ground surface, and panel under investigation into patches that emit and/or receive light [7]. Rays that connect light sources with receiving patches are checked for intersection with scene shading elements, such as panels, frames, racking, torque tubes, and posts. A front and rear IAM (defined by the user) are applied to the irradiance of each module-incident ray according to the AOI; for the results demonstrated here, we applied the IAM values calculated in the previous section to the front and rear illumination.

The AMM (Fig. 5) was assumed constant for direct, diffuse, and reflected light sources in a given time stamp and multiplied with the encapsulated cell responsivity (at AM1.5G, 0˚ AOI) to adjust the short circuit current of each cell. The temperature-adjusted single-diode model gives cell current-voltage (*I-V*) curves from which a module maximum power point is calculated based on the specified cell interconnections.

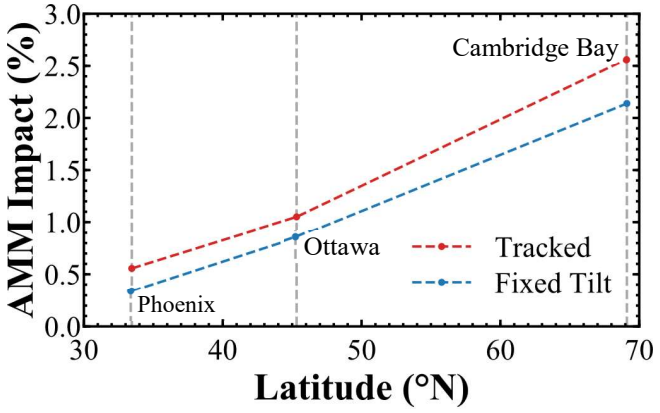

Fig. 6. Annual change in energy yield caused by the air mass modifier in Cambridge Bay, Ottawa, and Phoenix for the central module in an array with 5 rows and 21 modules per row in fixed latitude-tilt and single-axis tracked configurations.

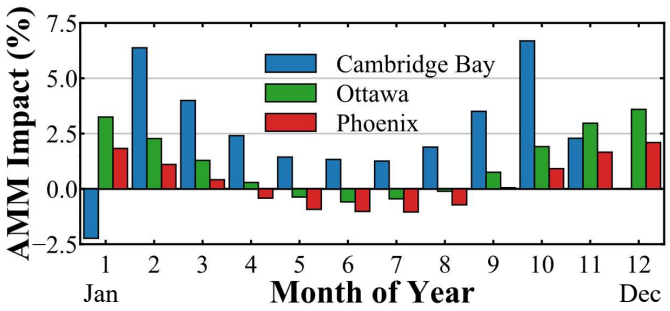

Fig. 7. Seasonal change in predicted energy yield caused by the air mass modifier for Fig. 1 module design under fixed latitude-tilt configuration. Note that there is no irradiance in Cambridge Bay in December.

B. Impact of Air Mass Modifier

The air-mass-modified energy yield was calculated from a typical meteorological year for a fixed latitude-tilt module at the center of an equator-facing array with 5 rows and 21 panels per row. This yield was compared to that of a module in the same configuration but without influence from the air mass (i.e. AMM = 1). The AMM impact is defined as:

$$\text{AMM Impact} = \frac{EY_{\text{AMM}} - EY_{\text{NoAMM}}}{EY_{\text{NoAMM}}} \quad (3)$$

where EY_{NoAMM} is the energy yield of the installation with no air mass modifier applied, and EY_{AMM} is the energy yield of the installation with the air mass modifier applied. Fig. 6 presents the AMM impact for three locations (Cambridge Bay, Nunavut, Canada; Ottawa, Ontario, Canada; and Phoenix, Arizona, USA) for a typical meteorological year.

For both fixed latitude-tilt and horizontal North-South single-axis tracking systems, the AMM increases predicted energy yield. The impact of increased cell absorption at high air masses becomes more significant with increasing latitude, since northern regions experience a greater number of high air mass hours. For the fixed latitude-tilt system, the AMM impact increases from 0.3% in Phoenix (33˚N), to 0.8% in Ottawa (45˚N), up to 2.1% in Cambridge Bay (69˚N).

The impact of air mass on predicted energy yield for a fixed-tilt system in Cambridge Bay (~2.1% gain) is in the same order of magnitude as electrical mismatch loss in some locations (0-1.5% loss) [14]. This indicates that module-specific AMM should be considered in high-latitude energy yield calculations.

In addition, the single-axis tracked installation shows a larger increase in energy yield compared to the fixed-tilt system when the AMM is applied due to an increased contribution of energy from high air mass hours in the early morning and late evening.

Air mass correction also has a more significant impact on energy yield outside summer months, as seen in Fig. 7. This effect is due to a higher average air mass in winter, which follows from larger average sun zenith angles. A similar pattern has been reported elsewhere for low-latitude locations [6]. This trend is more pronounced in high-latitude locations: Cambridge Bay has a peak monthly AMM impact of >6.5% in October,

while Ottawa and Phoenix show peaks of >3.6% and >2.1%, respectively, in December.

While AMM impact is typically positive in the winter months due to high average air masses, for Cambridge Bay the months of January and November show a reduced AMM impact due to a high proportion of very high air mass hours where the AMM is less than 1 (in January, the average GHI-weighted air mass is >AM20). The number of light-hours during these months is low, however; in January, the average day length is less than 1.3 hours, and the sun is below the horizon from November 24 to January 18.

CONCLUSION

A bifacial silicon heterojunction module was modeled optically in SunSolve, and its incidence angle modifier and air mass modifier were calculated. Sources of optical loss with respect to wavelength in the module were also presented.

At 80º angle of incidence, J_{sc} was reduced by 36%. Increased reflectivity was the dominant effect in reduced high-angle performance. The calculated incidence angle modifier was independent of air mass, within ~0.1% absolute for all air masses studied (AM1-AM38).

At high air masses (AM2-AM18), the module demonstrated an increase in normalized J_{sc} compared to the reference air mass (AM1.5), primarily due to reduced parasitic absorption and increased spectral responsivity at long wavelengths.

The modeled incidence angle modifier and air mass modifier of this module were incorporated in the SUNLAB's energy yield modelling software, DUET. The impact of air mass on energy yield is more significant for high-latitude locations due to higher average air masses. From these results, we can infer that air mass impacts in the range of 0.8-1.6% can be expected in other mid-latitude locations (45-60ºN), such as much of continental Europe.

The predicted energy yield of a fixed latitude-tilt panel in Cambridge Bay (69°N) increased by over 2.1% annually and 6.5% monthly, compared to air mass independent performance. These results suggest that, while air mass is often neglected in energy yield predictions at low latitudes, its impact should be considered for energy yield calculations in high latitude locations.

REFERENCES

[1] K. Yoshikawa, H. Kawasaki, W. Yoshida, T. Irie, K. Konishi, K. Nakano, T. Uto, D. Adachi, M. Kanematsu, H. Uzu, and K. Yamamoto, "Silicon heterojunction solar cell with interdigitated back contacts for a photoconversion efficiency over 26%," *Nat. Energy*, vol. 2, no. 5, 2017, doi: 10.1038/nenergy.2017.32.

[2] D. L. King, J. A. Kratochvil, and W. E. Boyson, "Measuring solar spectral and angle-of-incidence effects on photovoltaic modules and solar irradiance sensors," in *IEEE 26th Photovoltaic Specialist Conference (PVSC)*, 1997, pp. 1113–1116, doi: 10.1109/pvsc.1997.654283.

[3] W. De Soto, S. A. Klein, and W. A. Beckman, "Improvement and validation of a model for photovoltaic array performance," *Sol. Energy*, vol. 80, no. 1, pp. 78–88, 2006, doi: 10.1016/j.solener.2005.06.010.

[4] D. L. King, W. E. Boyson, and J. A. Kratochvil, "Analysis of factors influencing the annual energy production of photovoltaic systems," in *IEEE 29th Photovoltaic Specialist Conference (PVSC)*, 2002, pp. 1356–1361, doi: 10.1109/pvsc.2002.1190861.

[5] C. R. Osterwald, K. A. Emery, and M. Muller, "Photovoltaic module calibration value versus optical air mass: the air mass function," *Prog. Photovoltaics Res. Appl.*, vol. 22, pp. 560–573, 2014, doi: 10.1002/pip.

[6] G. S. Kinsey, "Spectrum sensitivity, energy yield, and revenue prediction of PV modules," *IEEE J. Photovoltaics*, vol. 5, no. 1, pp. 258–262, 2015, doi: 10.1109/JPHOTOV.2014.2370256.

[7] C. E. Valdivia, C. T. Li, A. Russell, J. E. Haysom, R. Li, D. Lekx, M. M. Sepeher, D. Henes, K. Hinzer, and H. P. Schriemer, "Bifacial Photovoltaic Module Energy Yield Calculation and Analysis," in *IEEE 44th Photovoltaic Specialist Conference (PVSC)*, 2017, pp. 1094–1099.

[8] PV Lighthouse, "SunSolve." [Online]. Available: https://www.pvlighthouse.com.au/.

[9] K. R. McIntosh, M. D. Abbott, B. A. Sudbury, S. Manzoor, Z. J. Yu, M. Leilaeioun, J. Shi, and Z. C. Holman, "Absorption in each layer of a silicon heterojunction solar cell," in *IEEE 44th Photovoltaic Specialist Conference (PVSC)*, 2017, pp. 1322–1328, doi: 10.1109/PVSC.2017.8366630.

[10] M. R. Lewis, E. M. Tonita, C. E. Valdivia, R. J. K. Obhi, J. Leslie, M. I. Bertoni, and K. Hinzer, "Angular Dependence of Textured Bifacial Silicon Heterojunction Solar Cells for High Latitudes," in *IEEE 46th Photovoltaic Specialist Conference (PVSC)*, 2019, pp. 1919–1923, doi: 10.1109/PVSC40753.2019.8980857.

[11] M. Lee and A. Panchula, "Spectral correction for photovoltaic module performance based on air mass and precipitable water," in *IEEE 43rd Photovoltaic Specialist Conference (PVSC)*, 2016, pp. 1351–1356, doi: 10.1109/PVSC.2016.7749836.

[12] M. Bliss, T. R. Betts, and R. Gottschalg, "Indoor measurement of photovoltaic device characteristics at varying irradiance, temperature and spectrum for energy rating," *Meas. Sci. Technol.*, vol. 21, no. 11, 2010, doi: 10.1088/0957-0233/21/11/115701.

[13] E. M. Tonita, C. E. Valdivia, and K. Hinzer, "Study of carrier transport in bifacial silicon heterojunction solar cells under high air mass illumination," in *IEEE 47th Photovoltaics Specialists Conference (PVSC)*, 2020.

[14] C. Deline, S. Ayala Pelaez, S. MacAlpine, and C. Olalla, "Bifacial PV System Mismatch Loss Estimation & Parameterization," in *36th EU PVSEC*, 2019, [Online]. Available: https://www.nrel.gov/docs/fy20osti/73541.pdf.

Chapter 5

Impact of Air Mass and Measured Spectra on Silicon Heterojunction Module Energy Yield in High-Latitude Locations

5.1 Preface

The following article has not yet been published. It is presented here in draft form.

This chapter expands upon some of the calculations performed in chapter 4, demonstrating annual and seasonal impact of air mass on energy yield of fixed-tilt and single-axis-tracked systems for more North American cities. The air mass modifier calculated in chapter 4 is applied again here, and figures 5.5 and 5.6 show results for eight locations with varying latitudes, rather than the original three shown in chapter 4. The impact of the air mass modifier is compared to the impact of the spectral correction factor, which corrects for changing module performance under measured spectra.

5.2 Introduction

Many northern and remote communities rely on diesel fuel for all their energy needs, including heating, transportation, and electricity. High transportation and operation costs in remote locations result in electricity prices up to $1.14/kWh in some communities [2], compared to the Canadian average of $0.14/kWh [3]. Reliance on diesel also has a negative impact on community health and the local environment [53]. Bifacial photovoltaics, photovoltaic (PV) modules that absorb light from both the front and rear sides, present a clean and low-cost alternative to diesel energy.

Bifacial gain, the increase in energy yield from additional irradiance absorbed by the module's rear face, varies based on environmental and site conditions [54][55]. In some cases, bifacial panels can produce up to 30% more energy than traditional monofacial panels under the same environmental

conditions and site setup [56]. High-latitude locations have potential for large bifacial gains, due to high albedo caused by snow cover and a high proportion of diffuse light.

Silicon heterojunction (SHJ) solar cells currently hold the record for silicon solar cell efficiency, at 26.7% [27], and are easily adaptable to bifacial applications [28]. However, these cells are typically characterized under the standard ASTM G-173-03 spectrum, which represents the solar spectrum under air mass 1.5 and clear-sky conditions [12].

Spectral shift is not typically accounted for in energy yield prediction software, although it can have a significant impact on results [57][58][59]. Some factors that affect the solar spectrum, such as air mass, become more significant with increasing latitude. In this paper, we explore the impact of two correction factors for a silicon heterojunction bifacial module: one based on modeled spectral data with varying air mass, and another based on measured spectral data.

While measured spectral data will provide the most accurate spectral correction for energy yield calculations, it is not always available. Energy yield correction based on air mass is comparatively simple to implement, and may offer a good approximation of correction based on measured spectra. In this paper, we evaluate air mass correction as a potential approximation of measured spectral correction. We analyze the effect that both correction factors have on energy yield calculations with respect to latitude.

5.3 Optical Model and Results

5.3.1 Optical Model of Module

Simulations of the solar module optical behavior were performed using SunSolve, a Monte Carlo ray-tracing software from PV Lighthouse that evaluates optical effects in thin-film and surface-textured devices. Figure 5.1 depicts the bifacial silicon heterojunction module layer structure used in our model, which includes ellipsometry data for thin-film layers, described in [60]. Simulations were run in 10-nm steps over the wavelength range of 300-1200 nm with a total of 5×10^6 rays.

For all results described in this paper, the short-circuit current was calculated as follows:

$$J_{sc} = \int SR(\lambda)E(\lambda)d\lambda \tag{5.1}$$

where J_{sc} is the short-circuit current in A/m^2, SR is the spectral response in A/W, E is the incident spectrum in W/m^2/nm, and λ is the wavelength in nm. The spectral response of the cell or module is determined from the external quantum efficiency (EQE) as:

$$SR(\lambda) = \frac{q\lambda}{hc}EQE(\lambda) \tag{5.2}$$

where q is the elementary charge in C, λ is the wavelength in m, h is the Plank constant in J·s, c is the speed of light in m/s, and EQE is the external quantum efficiency of the module.

The measured EQE of a bare silicon heterojunction cell, adjusted for anticipated shading losses, was compared to the simulated EQE of a bare SHJ cell (the structure in Figure 5.1, with ethylene vinyl

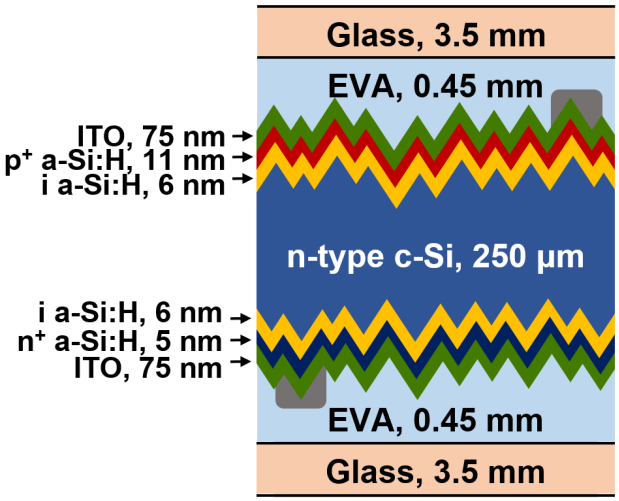

Figure 5.1: Schematic of the simulated bifacial SHJ module layer structure. c-Si: crystalline silicon, EVA: ethylene vinyl acetate, a-Si:H: hydrogenated amorphous silicon, ITO: indium tin oxide.

acetate (EVA) and glass layers removed) in SunSolve. The short-circuit current density (J_{sc}) was obtained by integrating these EQE with the standard AM1.5G spectrum, as described in equation 5.1. The resulting difference in J_{sc} was less than 1%, showing good agreement [61].

5.3.2 Air Mass Modifier

The air mass modifier (AMM) is a modifier that accounts for the module's change in performance under different air mass spectra due to changing spectral shape. With increasing air mass, UV irradiance is reduced by increased Rayleigh scattering for short wavelengths [62]. Each module design has a unique response to changing incident spectra, and consequently has a unique AMM [63]. The air mass modifier is defined as:

$$AMM = \frac{J_{\text{sc,AMX}}}{J_{\text{sc,ref}}} \times \frac{Irr_{\text{ref}}}{Irr_{\text{AMX}}} \tag{5.3}$$

where AMM is the air mass modifier, $J_{\text{sc,AMX}}$ is the short-circuit current of the module under a spectrum with air mass X, $J_{\text{sc,ref}}$ is the short-circuit current under the reference spectrum, Irr_{ref} is the total irradiance of the reference spectrum (280-4000 nm), and Irr_{AMX} is the total irradiance of a spectrum with air mass X (280-4000 nm). An AMM larger than one indicates that module short-circuit current under the test spectrum will be greater than that under the reference spectrum for the same integrated irradiance. In this paper, the reference spectrum is the ASTM AM1.5G standard spectrum [12].

To simulate high air mass conditions, spectra with varying air masses were generated by SMARTS [40]. These spectra followed the ASTM standard, varying only the relative air mass parameter. J_{sc} was calculated by integrating the modeled module EQE with the SMARTS spectrum at different air masses as described in equation 5.1. Total incident irradiance decreases with increasing air

mass, thereby reducing J_{sc}; this result is normalized by the irradiance (second part of equation 5.3) to isolate the impact of spectral shift.

The resulting AMM is shown in figure 5.2. AMM for air masses greater than 20 was assumed to be equal to the AMM at AM20. These very high air masses apply to a small fraction of total incident irradiance and so the effect of this approximation is assumed negligible.

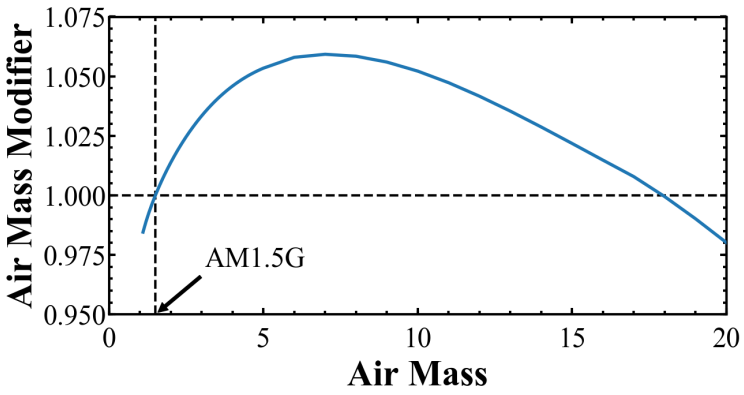

Figure 5.2: Air mass modifier for figure 5.1 module under AM1.1 to AM20 (AM1.5 indicated).

Absorption in the module's glass, EVA, and a-Si:H layers causes high parasitic absorption in the short-wavelength range [61]. As air mass increases, the spectrum has a smaller proportion of short-wavelength light, resulting in less parasitic absorption and an increase in the AMM. Past AM5, the parasitic absorption increases due to long-wavelength absorption by the ITO, EVA, and glass layers, and the AMM decreases. In addition, as air mass increases, light escape increases due to poor absorption of long-wavelength light in silicon, further reducing the AMM at high air masses [61].

5.4 Spectral Measurements and Spectral Model

5.4.1 SolarSIM-G Measurement System and CanSIM data

The SolarSIM-G is a cost-effective replacement for a spectroradiometer that uses nine narrow-wavelength channel measurements to model the global spectral irradiance from 280-4000 nm [44]. Its counterpart, the SolarSIM-D2, models direct irradiance from six channels and was validated in [45].

The CanSIM network is a deployment of spectral measurement devices to a number of cities in Canada, including seven stations in six provinces [64]. CanSIM stations include a SolarSIM-G to measure global horizontal spectral irradiance and a SolarSIM-D2 to measure direct normal spectral irradiance. Diffuse spectral irradiance can be calculated from these two spectral components, and the total GHI, DHI, and DNI can be found by integrating the spectral irradiance across the solar spectrum. These devices also measure the ambient temperature, humidity, and pressure. Pyranometers located at the CanSIM stations showed good agreement with SolarSIM-G integrated irradiance, within 2% [64]. CanSIM station data is logged in 1-minute intervals. Table 5.1 lists the locations for which CanSIM data was used in this paper.

Location	Coordinates
Egbert, ON	79.8° W, 44.2° N
Ottawa, ON	75.7° W, 45.4° N
Varennes, QC	73.4° W, 45.6° N
Charlottetown, PE	63.1° W, 46.3° N
Devon, AB	113.7° W, 53.4° N

Table 5.1: Locations with Spectral CanSIM data used in this paper.

At this time, the spectral data available is for latitudes of 44.2°N to 53.4°N. There is a CanSIM station in Cambridge Bay, Nunavut (69.1°N), that will have a full year of data available in the fall of 2020. Future work will include Cambridge Bay data in our studies of high-latitude spectral correction.

5.4.2 Spectral Correction Factor

The spectral correction factor (SCF) is a modifier that can be applied to energy yield models to account for the impact of spectra on module short-circuit current. While the AMM accounts for the effect of air mass on module performance, the SCF is calculated based on measured spectral data, and therefore accounts for all spectral effects, including air mass, water vapour, ozone, particulate matter, and clouds. In this paper, the SCF is calculated for each timestamp based on measured spectra provided by the CanSIM network. The SCF is defined as:

$$SCF = \frac{J_{\text{sc,test}}}{J_{\text{sc,ref}}} \times \frac{Irr_{\text{ref}}}{Irr_{\text{test}}} \tag{5.4}$$

where $J_{\text{sc,test}}$ is the short-circuit current of the module under a measured spectrum, $J_{\text{sc,ref}}$ is the short-circuit current under the reference spectrum, Irr_{ref} is the total irradiance of the reference spectrum, and Irr_{test} is the total irradiance of the measured spectrum.

By applying the SCF, the impact of changing spectral shape on short-circuit current is quantified, normalizing for the difference in total incident irradiance.

5.5 Comparison Between Spectral Correction Factor and Air Mass Modifier

The air mass modifier and the spectral correction factor are expected to vary considerably depending on the weather and atmospheric conditions. Figure 5.3 shows the SCF and AMM in Ottawa, Ontario for a sunny and a cloudy day in June, 2019. Since clouds affect the solar spectrum considerably, the SCF on the cloudy day shows much more variation from the AMM than on the sunny day. In addition, the AMM is based on SMARTS-generated spectra; SMARTS is a clear-sky model without any cloud modelling, so measured cloudy spectra can be expected to deviate considerably from modeled SMARTS spectra.

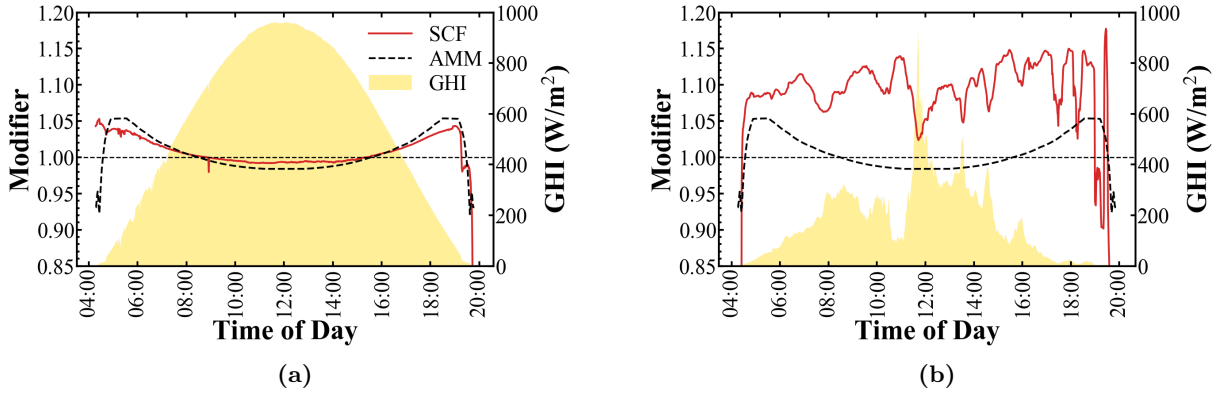

Figure 5.3: Spectral correction factor (SCF, red solid line), air mass modifier (AMM, black dashed line), and global horizontal irradiance (GHI, yellow fill) for a) a sunny day (June 6, 2019), and b) a cloudy day (June 13, 2019) in Ottawa, ON.

Timestamps' sky clearness index, ϵ, was calculated as defined by Perez in [43] and [42]:

$$\epsilon = \frac{\frac{DNI+DHI}{DHI} + \kappa\theta^3}{1 + \kappa\theta^3} \tag{5.5}$$

where θ is the zenith angle, in radians, and κ is a constant ($\kappa = 1.041$). The ϵ values allow the timestamps to be categorized in bins, as shown in table 5.2, where 1 is the cloudiest bin and 8 is the clearest bin.

ϵ Bin	Lower Bound	Upper Bound
1 (Overcast)	1	1.065
2	1.065	1.230
3	1.230	1.5
4	1.5	1.95
5	1.95	2.8
6	2.8	4.5
7	4.5	6.2
8 (Clear)	6.2	-

Table 5.2: Sky clearness categories based on ϵ, sky clearness.

In Ottawa in 2019, for the cloudiest timestamps (ϵ bin 1), the GHI-weighted average difference between the AMM and SCF is -0.05 (the AMM is 0.05 less than the SCF, on average). For the sunniest timestamps (ϵ bin 8), the GHI-weighted average difference is +0.003. Therefore, the AMM tends to underestimate the SCF on cloudier days and overestimate the SCF on sunny days, as is the case for the days shown in figure 5.3. There is also a larger average error when applying the AMM on cloudy days compared to sunny days. The difference between these correction factors may be due to atmospheric effects not accounted for in the AMM; clouds, in particular, are not modeled in the SMARTS spectra that were used to calculate the AMM.

The spectral data of a sunny and a cloudy timestamp are shown in figure 5.4. Figure 5.4a shows

a typical sunny timestamp, with an air mass of 1.1, a SCF of 0.99, and 958 W/m^2 of irradiance. This timestamp has an SCF of less than one due to its high UV content, causing increased parasitic absorption and thermalization losses compared to the reference spectrum.

The cloudy timestamp (figure 5.4b) has equal diffuse and global horizontal irradiance (GHI=DHI), with direct irradiance equal to zero (DNI=0). The air mass is 1.1, SCF is 1.1, and the irradiance is 110 W/m^2. This measured spectrum deviates considerably from the SMARTS-generated AM1.1G spectrum used to calculated the air mass modifier. Diffuse irradiance is blue-shifted compared to direct irradiance due to absorption of long-wavelength light in clouds and increased scattering of blue light in the atmosphere [65]. Therefore, there is reduced irradiance in the long-wavelength region with energy below the silicon bandgap; this reduces light escape, resulting in a higher SCF. While the SCF is high for cloudy days, the total irradiance is typically low, so cloudy days have a smaller impact on total predicted energy yield than sunny days.

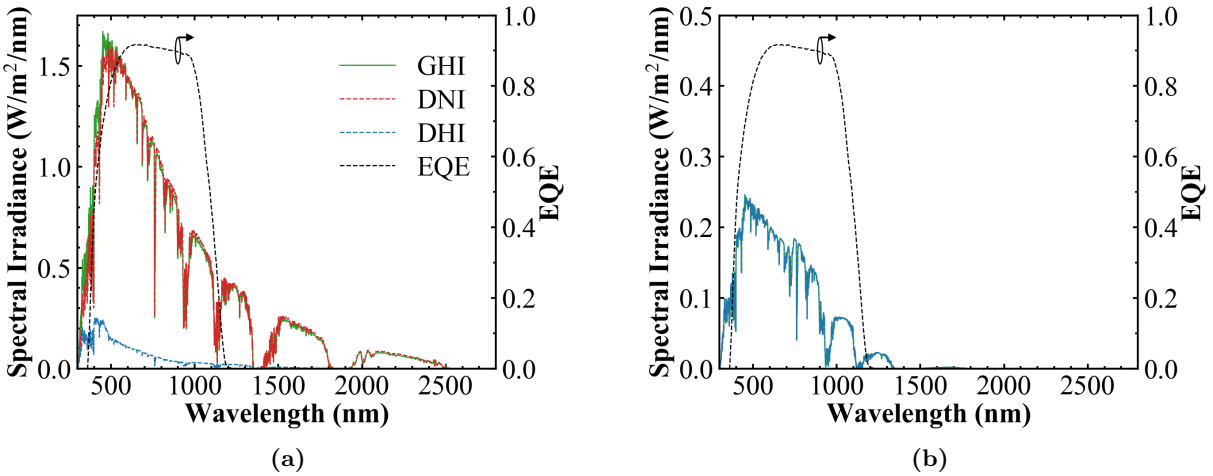

Figure 5.4: Global horizontal irradiance (GHI, green solid line), direct normal irradiance (DNI, red dashed line), diffuse horizontal irradiance (DHI, blue dashed line), and external quantum efficiency of the silicon heterojunction module (EQE, black dashed line) for a) a sunny timestamp (12:00, June 6, 2019), and b) a cloudy timestamp (11:00, June 13, 2019) in Ottawa, ON.

5.6 Impact of Spectral Correction on Energy Yield

The SUNLAB's energy yield prediction software, DUET, uses a combination of a 3D view-factor model and a ray-intersection shading algorithm to predict the energy yield of a fixed-tilt or single-axis-tracked bifacial solar panel. The model generates cell I-V curves from a temperature-adjusted single-diode model. A module maximum power point is calculated based on the specified cell interconnection.

The energy yield was predicted for a 5 row, 21 module per row installation in both fixed-tilt and single-axis-tracked configurations. The AMM and SCF were incorporated in the DUET software by applying them to the module's responsivity, effectively changing the module's modeled efficiency. The simulated incidence angle modifier of this module was also incorporated in the DUET calculations, as described in [61].

5.6.1 Impact of Air Mass Modifier on Energy Yield

Energy yield was calculated with and without the AMM for eight cities with increasing latitude, listed in Table 5.3. Cities were selected with a range of latitudes from 30°N to 70°N. Energy yield calculations were based on Typical Meteorological Year (TMY) and Canadian Weather Year for Energy Calculation (CWEC) datasets.

For Canadian locations, the albedo was calculated on a monthly basis based on average snow coverage information included in the CWEC dataset, with an albedo of 0.6 for snow cover and 0.2 for grass (no snow cover). Albedo was taken directly from the TMY datasets for American locations.

Since TMY and CWEC data is available for a wider range of locations while the CanSIM data available follows a narrower range of latitudes, the locations chosen do not follow the CanSIM dataset exactly. There are two cities that overlap between the datasets (Devon, AB, and Edmonton, AB are in the same municipality).

Location	Coordinates
Phoenix, AZ	112.07° W, 33.45° N
Albuquerque, NM	106.62° W, 33.04° N
Denver, CO	104.99° W, 39.83° N
Ottawa, ON	75.70° W, 45.32° N
Moosonee, ON	80.60° W, 51.23° N
Edmonton, AB	113.58° W, 53.31° N
Yellowknife, YT	114.44° W, 62.46° N
Cambridge Bay, NU	105.14° W, 69.11° N

Table 5.3: Locations for air mass impact calculation.

The impact of the air mass modifier was defined as:

$$AMM\ Impact = \frac{EY_{\mathrm{AMM}} - EY_{\mathrm{noAMM}}}{EY_{\mathrm{noAMM}}} \tag{5.6}$$

where EY_{AMM} is the predicted energy yield when the air mass modifier is applied, and EY_{NoAMM} is the predicted energy yield with no air mass modifier applied.

The AMM impact increases with increasing latitude for both fixed-tilt and single-axis tracked systems, as shown in figure 5.5. This is caused by higher average air mass with increasing latitude: Cambridge Bay has an irradiance-weighted average air mass of 3.1, while Phoenix has a weighted average air mass of 1.8. The single-axis-tracked energy yield also shows an increased AMM impact when compared to fixed-tilt installations due to a larger energy yield contribution from high air mass hours in the morning and evening.

The impact of air mass also varies seasonally, with a higher impact in winter months compared to summer months. This is a result of the larger proportion of high air mass hours in the winter. Monthly AMM impact for a fixed-tilt installation is shown in figure 5.6. Note that there is no irradiance in Cambridge Bay in December. In January and November in Cambridge Bay, and

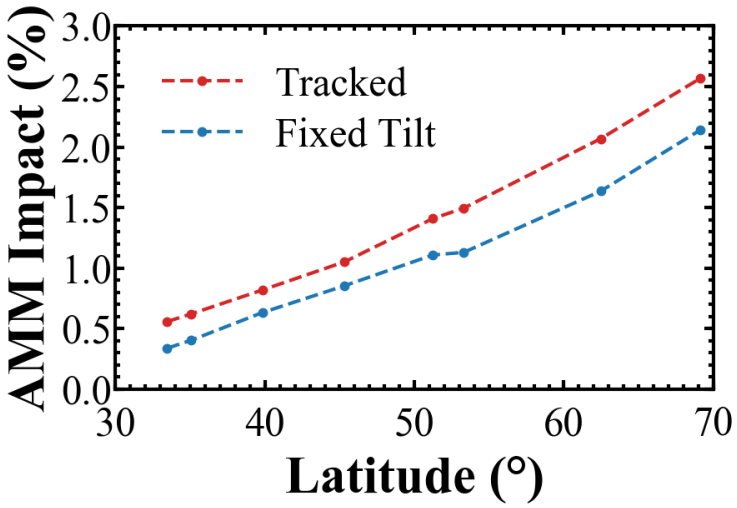

Figure 5.5: Annual change in energy yield caused by the air mass modifier of module depicted in figure 5.1 for select cities in North America. The installation has 5 rows and 21 modules per row in latitude fixed-tilt (blue) and single-axis tracked (red) configurations.

in December in Yellowknife, very high air mass values (>AM18) cause some AMM values less than 1, resulting in decreased AMM impact. In addition, for many low-latitude cities, low average summertime air masses (<AM1.5) cause many AMM values less than 1, resulting in negative AMM impact in the summer months.

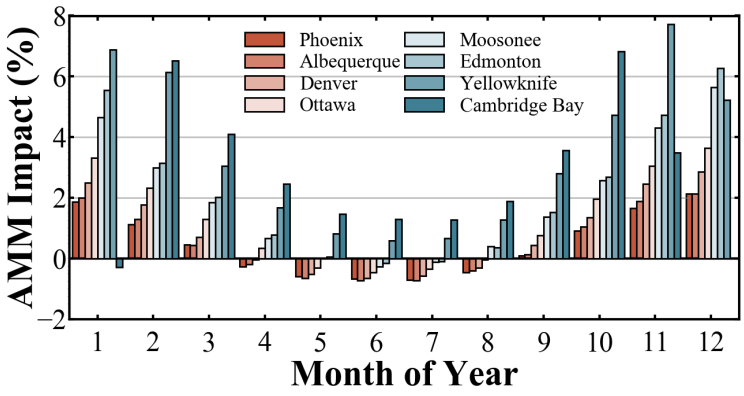

Figure 5.6: Seasonal change in energy yield for a latitude fixed-tilt installation caused by the air mass modifier of the module depicted in figure 5.1 for select cities in North America.

5.6.2 Impact of Spectral Correction Factor on Energy Yield

Energy yield was calculated for the cities listed in table 5.3 for three cases: with no correction factor, with the air mass modifier (figure 5.2), and with the spectral correction factor.

The spectral correction factor impact is defined as follows:

$$SCF\ Impact = \frac{EY_{\mathrm{SCF}} - EY_{\mathrm{noSCF}}}{EY_{\mathrm{noSCF}}} \tag{5.7}$$

where EY_{SCF} is the energy yield with the spectral correction factor applied, and EY_{NoSCF} is the energy yield without the spectral correction factor. This can be calculated for any number of timestamps by taking their total energy yield with and without the SCF applied.

The annual SCF impact and AMM impact of CanSIM cities is shown in figure 5.7a. The AMM impact is similar between the first four cities due to their similar latitude (44.2°N - 46.3°N).

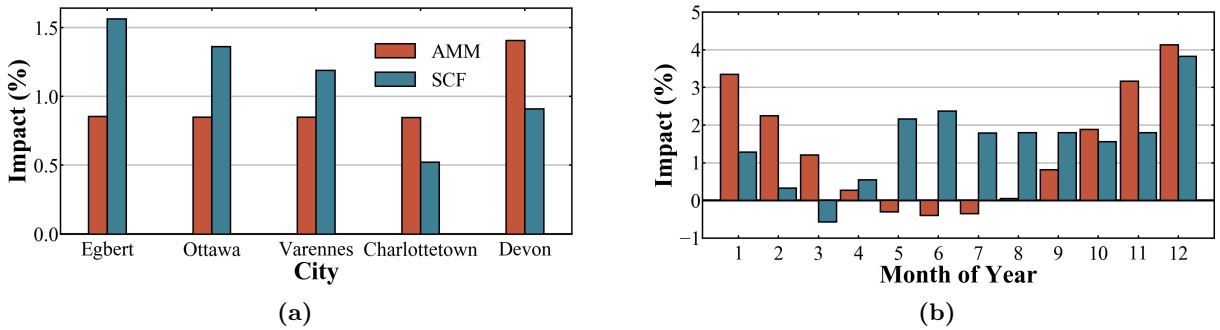

Figure 5.7: Energy yield impact of air mass modifier (AMM) and spectral correction factor (SCF) for a) various cities on an annual basis and b) Ottawa, ON, on a monthly basis.

On an annual basis, the AMM brought the energy yield closer to the SCF-corrected energy yield for all cities, as shown in figure 5.7a. However, on shorter timescales, the impact of the AMM and the SCF differ considerably. This supports the common assumption that, on an annual basis, most seasonal and daily spectral variations due to changing environmental conditions are effectively averaged out [66].

Figure 5.7b shows the monthly AMM and SCF impact for Ottawa, ON. The SCF impact in the summer months is much larger than the AMM impact; while the AMM impact is negative due small average air masses (as explained in section 5.6.1) the SCF impact is positive. The cloudy timestamps in these months increase the SCF (and consequently the SCF impact). In addition, many high-irradiance hours during sunny days have a slightly higher SCF than AMM (see figure 5.3a); this may be due to spectral effects not accounted for in the AMM.

For shorter timescales, larger SCF and AMM impacts can be observed. For individual 1-minute timestamps, SCF impacts of up to 88% are observed, while the maximum per-timestamp AMM impact is 12%. These large SCF impact values generally only affect low irradiance timestamps (GHI<100 W/m^2). If low-irradiance timestamps are ignored, the maximum per-timestamp SCF and AMM impacts become 35% and 11%, respectively.

Although the AMM is an acceptable first approximation towards the SCF on an annual basis, it does not provide satisfactory agreement on seasonal or shorter timescales. Further investigation is required to determine what other factors, in addition to air mass, should be incorporated to better match the SCF at short timescales when implementing approximate spectral correction methods such as the AMM.

Since air mass is the most significant parameter affecting spectral shape, and air mass impact increases with latitude, we expect the SCF impact to increase with respect to latitude, as the AMM impact does; however, the energy yield impact is difficult to quantify without spectral data for a wider range of latitudes. Spectral data from at least one low-latitude location, as well as a full year of data from a high-latitude location, such as the CanSIM station in Cambridge Bay, is required for further study.

5.7 Conclusion

Air mass can have a significant impact on energy yield predictions for silicon heterojunction modules, and is especially important for high-latitude locations. When air mass is taken into account, energy yield predictions for a fixed-tilt module increased by over 6.8% monthly and 2.1% annually for Cambridge Bay, NU (69.1°N), and by over 3.6% monthly and 0.8% annually for Ottawa, ON (45.4°N).

A spectral correction factor based on spectral measurements increased energy yield predictions of a fixed-tilt module by up to 1.35% annually and 4% monthly in Ottawa, ON. High-latitude locations are expected to demonstrate even higher spectral correction factor impact due to high air mass and high proportion of diffuse light.

While the air mass modifier can act as a first step towards spectral correction if spectral data is unavailable, it is only accurate on an annual basis, and may introduce error if applied on shorter timescales, especially on cloudy days.

Chapter 6

Conclusion

Bifacial photovoltaics present a promising alternative energy source for high-latitude remote communities that rely on diesel generators; however, predicting energy yield in these locations can be challenging due to the divergence of operating conditions from standard test conditions. This work sought to quantify silicon heterojunction cell and module performance under high-latitude conditions to reduce investment risk and facilitate solar energy adoption in high-latitude communities.

In chapter 3, the conference proceeding titled "Angular Dependence of Textured Bifacial Silicon Heterojunction Solar Cells for High Latitudes" describes the fabrication methodology that was used to create hydrogenated amorphous silicon and indium-tin-oxide thin films at Arizona State University's Solar Power Lab. Complex refractive indices for these materials, obtained via ellipsometry, were presented and incorporated in a SunSolve model of a silicon heterojunction solar cell. Results presented in this paper indicate that silicon heterojunction cells are ideal solar cells for high-latitude applications, because one of their primary design weaknesses - parasitic absorption in the UV region - becomes less significant as air mass increases.

In chapter 4, the conference proceeding titled "Impact of Air Mass on Energy Yield Calculation for Bifacial Silicon Heterojunction Photovoltaic Modules in High-Latitude Conditions" presents an adapted version of the SunSolve model from the previous chapter that represents a silicon heterojunction module. The module's incidence angle modifier and air mass modifier are calculated and incorporated in DUET, the SUNLAB's bifacial photovoltaic energy yield prediction software, to better represent module performance under Arctic conditions. As expected based on preliminary results in chapter 3, the module demonstrates increased efficiency under high air mass spectra, demonstrating that silicon heterojunction modules are well-suited to high-latitude applications. In addition, the impact of air mass on energy yield is shown to increase with increasing latitude: for a fixed latitude-tilt system, the annual air mass impact is $\sim$0.3% in Phoenix, AZ and $>$2% in Cambridge Bay, NU. This demonstrates that, while air mass is often neglected for low-latitude energy yield calculations, it should be considered for high latitude locations.

Chapter 5 presents a paper draft titled "Impact of Air Mass and Measured Spectra on Silicon Heterojunction Module Energy Yield in High-Latitude Locations." In this paper, the spectral correction factor, a modifier that accounts for changing module performance under arbitrary spectra, is introduced. The impact of spectral correction on energy yield, based on reconstructed solar spectra for five cities in Canada, is calculated. The air mass modifier presented in chapter 4 is then applied to energy yield calculations for the same five cities and the air-mass-corrected energy yield

is compared to the spectrally-corrected energy yield. For these locations, the air mass modifier is shown to improve agreement with spectrally-corrected predicted energy yield on an annual basis; however, on a shorter timescale, especially for cloudy timestamps, changes in measured spectra are not well-represented by the air mass modifier. Further work investigating changes in spectral shape due to other atmospheric factors is required.

The results presented here indicate a few important improvements and further topics for investigation. A wider variety of spectral measurement data should be obtained and analyzed, including measured spectral data for a low-latitude location and a full year of spectral data for Cambridge Bay (or an equally high-latitude location). Furthermore, analyzing other atmospheric factors, such as clearness index, precipitable water, and ozone, may improve energy yield calculations without access to measured spectral data. Moving forward, we intend to validate our energy yield predictions with measurements from the SUNLAB's field test stations in Ottawa, Ontario, and Cambridge Bay, Nunavut.

Although more work is required to quantify bifacial solar module performance under high-latitude spectra, these results demonstrate that silicon heterojunction cells and modules are a strong choice for high-latitude solar module installations.

References

[1] Natural Resources Canada, *The Atlas of Canada - Remote Communities Energy Database*, 2018. [Online]. Available: http://atlas.gc.ca/rced-bdece/en/index.html (visited on 07/15/2019).

[2] WWF Canada, "Tracking Diesel Fuel Subsidies in Nunavut," Tech. Rep., 2017, p. 32. [Online]. Available: http://assets.wwf.ca/downloads/costing%7B%5C_%7Dfossil%7B%5C_%7Dfuel%7B%5C_%7Dsubsidies%7B%5C_%7Din%7B%5C_%7Dnunavut.pdf.

[3] Neven Valev, *Canada Electricity Prices*, 2020. [Online]. Available: https://www.globalpetrolprices.com/Canada/electricity%7B%5C_%7Dprices/ (visited on 05/25/2020).

[4] M. Brooks, N. Moore, H. Rutherford, J. Wright, and D. Bowman, "Energy Access - The Canadian Context," Tech. Rep. March, 2017. DOI: 10.1080/0965214002005383. [Online]. Available: http://wgsi.org/sites/wgsi-live.pi.local/files/Energy%7B%5C_%7DAccess%7B%5C_%7DCanadian%7B%5C_%7DContext%7B%5C_%7DInfographic%7B%5C_%7DSpread-OpenAccess%7B%5C_%7DEnergy%7B%5C_%7DBlueprint%7B%5C_%7DWGSI%7B%5C_%7D2017.pdf.

[5] Treasury Board of Canada Secretariat, *Federal contaminated sites inventory*, 2020. [Online]. Available: https://www.tbs-sct.gc.ca/fcsi-rscf/home-accueil-eng.aspx (visited on 05/12/2020).

[6] N. C. Mcdonald and J. M. Pearce, "Renewable Energy Policies and Programs in Nunavut : Perspectives from the Federal and Territorial Governments," *Arctic*, vol. 65, no. 4, pp. 465–475, 2018.

[7] Energyhub.org, *Cost of Solar Power In Canada 2020*, 2020. [Online]. Available: https://www.energyhub.org/cost-solar-power-canada/ (visited on 08/07/2020).

[8] Canada Energy Regulator (CER), "The Economics of Solar Power in Canada," Tech. Rep., 2020. [Online]. Available: https://www.cer-rec.gc.ca/nrg/sttstc/lctrct/rprt/cnmcsfslrpwr/index-eng.html.

[9] Canada Energy Regulator, *Market Snapshot: Overcoming the challenges of powering Canada's off-grid communities*, 2018. [Online]. Available: https://www.cer-rec.gc.ca/nrg/ntgrtd/mrkt/snpsht/2018/10-01-1cndffgrdcmmnts-eng.html (visited on 05/12/2020).

[10] E. Maruyama, A. Terakawa, M. Taguchi, Y. Yoshimine, D. Ide, T. Baba, M. Shima, H. Sakata, and M. Tanaka, "Sanyo's Challenges to the Development of High-efficiency HIT Solar Cells and the Expansion of HIT Business," in *2006 IEEE 4th World Conference on Photovoltaic Energy Conversion*, IEEE, 2006, pp. 1455–1460, ISBN: 1424400163.

[11] S. Xiao and S. Xu, "High-efficiency silicon solar cells - Materials and devices physics," *Critical Reviews in Solid State and Materials Sciences*, vol. 39, no. 4, pp. 277–317, 2014, ISSN: 15476561. DOI: 10.1080/10408436.2013.834245.

[12] ASTM International, *G173-03 Standard Tables for Reference Solar Spectral Irradiances: Direct Normal and Hemispherical on 37 Tilted Surface*, West Conshohocken, PA, 2012. DOI: https://doi.org/10.1520/G0173-03R12.

[13] W. Shockley and H. J. Queisser, "Detailed balance limit of efficiency of p-n junction solar cells," *Journal of Applied Physics*, vol. 32, no. 3, pp. 510–519, 1961, ISSN: 00218979. DOI: 10.1063/1.1736034. arXiv: 9809069v1 [arXiv:gr-qc].

[14] S. Hubbard, "Absorption and Generation," in *Photovoltaic Solar Energy: From Fundamentals to Applications*, A. Reinders, P. Verlinden, W. van Sark, and A. Freundlich, Eds., West Sussex, UK: John Wiley & Sons, 2017, pp. 32–38.

[15] S. Hubbard, "Recombination," in *Photovoltaic Solar Energy: From Fundamentals to Applications*, A. Reinders, P. Verlinden, W. van Sark, and A. Freundlich, Eds., Sussex, UK: John Wiley & Sons Ltd., 2017, ch. Chapter 2. Pp. 39–46.

[16] R. V. Chavali, S. De Wolf, and M. A. Alam, "Device physics underlying silicon heterojunction and passivating-contact solar cells: A topical review," *Progress in Photovoltaics: Research and Applications*, vol. 26, no. 4, pp. 241–260, 2018, ISSN: 1099159X. DOI: 10.1002/pip.2959.

[17] X. Wang and Z. M. Wang, Eds., *High-Efficiency Solar Cells: Physics, Materials and Devices*. London, UK: Springer, 2014, vol. 190, p. 664, ISBN: 978-3-319-01987-1. DOI: 10.1007/978-3-319-01988-8. [Online]. Available: http://link.springer.com/10.1007/978-3-319-01988-8.

[18] T. Markvart and L. Castañer, "Principles of Solar Cell Operation," in *Practical Handbook of Photovoltaics*, L. Castañer, A. Mcevoy, and T. Markvart, Eds., Second Edi, Oxford, UK: Elsevier Ltd., 2013, ch. IA-1, pp. 3–25, ISBN: 9780123859341. DOI: 10.1016/B978-0-12-385934-1.00001-5. arXiv: arXiv:1011.1669v3.

[19] O. Breitenstein, J. P. Rakotoniaina, M. H. Al Rifai, and M. Werner, "Shunt types in crystalline silicon solar cells," *Progress in Photovoltaics: Research and Applications*, vol. 12, no. 7, pp. 529–538, 2004, ISSN: 10627995. DOI: 10.1002/pip.544.

[20] J. E. Castillo-Aguilella and P. S. Hauser, "Multi-Variable Bifacial Photovoltaic Module Test Results and Best-Fit Annual Bifacial Energy Yield Model," *IEEE Access*, vol. 4, pp. 498–506, 2016, ISSN: 21693536. DOI: 10.1109/ACCESS.2016.2518399.

[21] International Electrotechnical Commission, "IEC 60904: Photovoltaic devices – Part 1-2: Measurement of current-voltage characteristics of bifacial photovoltaic (PV) devices (Draft A)," Tech. Rep. [Online]. Available: pvpmc.sandia.gov/download/6029/.

[22] A. Schmid, G. Dülger, G. Baraah, U. Kräling, and F. Ise, "IV Measurement of Bifacial Modules: Bifacial vs. Monofacial Illumination," *33rd European Photovoltaic Solar Energy Conference and Exhibition*, no. September, pp. 1624–1627, 2017. DOI: 10.4229/EUPVSEC20172017-5BV.4.32.

[23] J. Libal and R. Kopecek, Eds., *Bifacial Photovoltaics: Technology, Applications and Economics*. London, UK: The Institution of Engineering and Technology, 2018, p. 304, ISBN: 9781785612749.

[24] M. T. Patel, M. R. Khan, X. Sun, and M. A. Alam, "A worldwide cost-based design and optimization of tilted bifacial solar farms," *Applied Energy*, vol. 247, no. April, pp. 467–479, 2019, ISSN: 03062619. DOI: 10.1016/j.apenergy.2019.03.150. [Online]. Available: https://doi.org/10.1016/j.apenergy.2019.03.150.

[25] ITRPV, "International Technology Roadmap for Photovoltaic (ITRPV), Ninth Edition," Tech. Rep. September, 2018. DOI: http://www.itrs.net/Links/2013ITRS/2013Chapters/2013Litho.pdf. [Online]. Available: www.itrpv.net..

[26] M. Tanaka, M. Taguchi, T. Matsuyama, T. Sawada, S. Tsuda, S. Nakano, H. Hanafusa, and Y. Kuwano, "Development of new a-Si/c-Si heterojunction solar cells: ACJ-HIT (artificially constructed junction-heterojunction with intrinsic thin-layer)," *Japanese Journal of Applied Physics*, vol. 31, no. 11R, p. 3518, 1992.

[27] K. Yoshikawa, H. Kawasaki, W. Yoshida, Toru Irie, K. Konishi, K. Nakano, and T. Uto, "Silicon heterojunction solar cell with interdigitated back contacts for a photoconversion efficiency over 26%," *Nature Energy*, vol. 2, no. 5, p. 17 032, 2017.

[28] C. Ballif, S. De Wolf, A. Descoeudres, and Z. C. Holman, "Amorphous Silicon/Crystalline Silicon Heterojunction Solar Cells," in *Advances in Photovoltaics: Part 3*, G. P. Willeke and E. R. Weber, Eds., Elsevier Inc., 2014, ch. Chapter 2, pp. 73–120, ISBN: 9780123884176. DOI: 10.1016/B978-0-12-388417-6.00003-9. [Online]. Available: https://linkinghub.elsevier.com/retrieve/pii/B9780123884176000039.

[29] L. Korte, E. Conrad, H. Angermann, R. Stangl, and M. Schmidt, "Advances in a-Si:H/c-Si heterojunction solar cell fabrication and characterization," *Solar Energy Materials and Solar Cells*, vol. 93, no. 6-7, pp. 905–910, 2009, ISSN: 09270248. DOI: 10.1016/j.solmat.2008.10.020.

[30] W. G. Van sark, F. Roca, and L. Korte, *Physics and technology of amorphous-crystalline heteronstrutures sillicon solar cells.* 2012, p. 588, ISBN: 9783642222740.

[31] F. Roca, J. Cárabe, and A. Jäger-Waldau, "Silicon Heterojunction Cells R&D in Europe," in *Proceedings of the 19th EU-PVSEC*, Orlando, USA, 2004.

[32] K. R. McIntosh, M. D. Abbott, B. A. Sudbury, S. Manzoor, Z. J. Yu, M. Leilaeioun, J. Shi, and Z. C. Holman, "Absorption in each layer of a silicon heterojunction solar cell," in *IEEE 44th Photovoltaics Specialists Conference (PVSC)*, Washington, DC, 2017, pp. 1322–1328. DOI: 10.1109/PVSC.2017.8366630.

[33] S. D'Elia, N. Scaramuzza, F. Ciuchi, C. Versace, G. Strangi, and R. Bartolino, "Ellipsometry investigation of the effects of annealing temperature on the optical properties of indium tin oxide thin films studied by Drude-Lorentz model," *Applied Surface Science*, vol. 255, no. 16, pp. 7203–7211, 2009, ISSN: 01694332. DOI: 10.1016/j.apsusc.2009.03.064.

[34] V. Sharma and S. S. Chandel, "Performance and degradation analysis for long term reliability of solar photovoltaic systems: A review," *Renewable and Sustainable Energy Reviews*, vol. 27, pp. 753–767, 2013, ISSN: 13640321. DOI: 10.1016/j.rser.2013.07.046. [Online]. Available: http://dx.doi.org/10.1016/j.rser.2013.07.046.

[35] World Meteorological Organization, "Guide to meteorological instruments and methods of observation: Volume I –Measurement of Meteorological Variables," Tech. Rep. 8, 2018.

[36] S. K. Kurinec, Ed., *Emerging Photovoltaic Materials*. Hoboken, NJ: John Wiley & Sons, Inc., 2018. DOI: 10.1002/9781119407690.

[37] D. R. Myers, *Solar Radiation: Practical Modeling for Renewable Energy Applications*, A. Ghassemi, Ed., 9. Boca Raton, FL: Taylor & Francis Group, 2013, vol. 53, ISBN: 9788578110796. DOI: 10.1017/CBO9781107415324.004. arXiv: arXiv:1011.1669v3.

[38] M. Sengupta, A. Habte, S. Kurtz, A. Dobos, S. Wilbert, E. Lorenz, T. Stoffel, D. Renné, C. Gueymard, D. Myers, S. Wilcox, P. Blanc, and R. Perez, "Best Practices Handbook for the Collection and Use of Solar Resource Data for Solar Energy Applications," Tech. Rep., 2015. DOI: 10.1016/j.solener.2003.12.003. [Online]. Available: https://www.nrel.gov/docs/fy15osti/63112.pdf.

[39] PV Lighthouse, *SunSolve*. [Online]. Available: https://www.pvlighthouse.com.au/.

[40] C. A. Gueymard, "SMARTS2: a simple model of the atmospheric radiative transfer of sunshine: algorithms and performance assessment," Tech. Rep., 1995, pp. 1–84. [Online]. Available: http://instesre.org/GCCE/SMARTS2.pdf.

[41] C. E. Valdivia, C. T. Li, A. Russell, J. E. Haysom, R. Li, D. Lekx, M. M. Sepeher, D. Henes, K. Hinzer, and H. P. Schriemer, "Bifacial Photovoltaic Module Energy Yield Calculation and Analysis," in *IEEE 44th Photovoltaic Specialists Conference (PVSC)*, Washington, DC, 2017, pp. 1094–1099.

[42] R. Perez, R. Seals, and J. Michalsky, "All-weather model for sky luminance distribution-Preliminary configuration and validation," *Solar Energy*, vol. 50, no. 3, pp. 235–245, 1993, ISSN: 0038092X. DOI: 10.1016/0038-092X(93)90017-I.

[43] R. Perez, P. Ineichen, R. Seals, J. Michalsky, and R. Stewart, "Modeling daylight availability and irradiance components from direct and global irradiance," *Solar Energy*, vol. 44, no. 5, pp. 271–289, 1990, ISSN: 0038092X. DOI: 10.1016/0038-092X(90)90055-H.

[44] V. Tatsiankou, K. Hinzer, H. Schriemer, P. McVey-White, and R. Beal, "Efficient, Real-Time Global Spectral and Broadband Irradiance Acquisition," in *IEEE 45th Photovoltaics Specialists Conference (PVSC)*, Waikoloa Village, HI, 2018, pp. 2362–2365, ISBN: 9781538685297. DOI: 10.1109/PVSC.2018.8547671.

[45] V. Tatsiankou, K. Hinzer, H. Schriemer, S. Kazadzis, N. Kouremeti, J. Gröbner, and R. Beal, "Extensive validation of solar spectral irradiance meters at the World Radiation Center," *Solar Energy*, vol. 166, no. March, pp. 80–89, 2018, ISSN: 0038092X. DOI: 10.1016/j.solener.2018.03.044. [Online]. Available: https://doi.org/10.1016/j.solener.2018.03.044.

[46] V. Tatsiankou, K. Hinzer, J. Haysom, H. Schriemer, K. Emery, and R. Beal, "Design principles and field performance of a solar spectral irradiance meter," *Solar Energy*, vol. 133, pp. 94–102, 2016, ISSN: 0038092X. DOI: 10.1016/j.solener.2016.03.054. [Online]. Available: http://dx.doi.org/10.1016/j.solener.2016.03.054.

[47] S. Y. Herasimenka, "Large Area Ultrapassivated Silicon Solar Cells Using Heterojunction Carrier Collectors," PhD thesis, Arizona State University, 2013, (Thesis).

[48] Y. Abdulraheem, I. Gordon, T. Bearda, H. Meddeb, and J. Poortmans, "Optical bandgap of ultra-thin amorphous silicon films deposited on crystalline silicon by PECVD," *AIP Advances*, vol. 4, no. 5, 2014, ISSN: 21583226. DOI: 10.1063/1.4879807.

[49] M. R. Vogt, H. Hahn, H. Holst, M. Winter, C. Schinke, M. Kontges, R. Brendel, and P. P. Altermatt, "Measurement of the Optical Constants of Soda-Lime Glasses in Dependence of Iron Content and Modeling of Iron-Related Power Losses in Crystalline Si Solar Cell Modules," *IEEE Journal of Photovoltaics*, vol. 6, no. 1, pp. 111–118, 2016, ISSN: 21563381. DOI: 10.1109/JPHOTOV.2015.2498043.

[50] K. R. McIntosh, J. N. Cotsell, J. S. Cumpston, A. W. Norris, N. E. Powell, and B. M. Ketola, "'An optical comparison of silicone and EVA encapsulants for conventional silicon PV modules: A ray-tracing study," *IEEE 34th Photovoltaic Specialist Conference (PVSC)*, no. June, 2009, ISSN: 01608371. DOI: 10.1109/PVSC.2009.5411624.

[51] H. T. Nguyen, F. E. Rougieux, B. Mitchell, and D. Macdonald, "Temperature dependence of the band-band absorption coefficient in crystalline silicon from photoluminescence," *Journal of Applied Physics*, vol. 115, no. 4, 2014, ISSN: 10897550. DOI: 10.1063/1.4862912.

[52] M. A. Green, "Self-consistent optical parameters of intrinsic silicon at 300 K including temperature coefficients," *Solar Energy Materials and Solar Cells*, vol. 92, no. 11, pp. 1305–1310, 2008, ISSN: 09270248. DOI: 10.1016/j.solmat.2008.06.009.

[53] Department of executive and Intergovernmental Affairs, "Ikummatiit: The Government of Nunavut Energy Strategy," Government of Nunavut, Iqaluit, Tech. Rep., 2007. [Online]. Available: http://www.gov.nu.ca/files/Ikummatiit%20Energy%20strategy%7B%5C_%7Dsept%202007%7B%5C_%7Deng.pdf.

[54] A. Asgharzadeh, S. Member, B. Marion, C. Deline, C. Hansen, J. S. Stein, and F. Toor, "A sensitivity study of the impact of installation parameters and system configuration on the performance of bifacial PV arrays," *IEEE Journal of Photovoltaics*, vol. 8, no. 3, pp. 798–805, 2018. DOI: 10.1109/JPHOTOV.2018.2819676.

[55] U. A. Yusufoglu, T. H. Lee, T. M. Pletzer, A. Halm, L. J. Koduvelikulathu, C. Comparotto, R. Kopecek, and H. Kurz, "Simulation of energy production by bifacial modules with revision of ground reflection," *Energy Procedia*, vol. 55, pp. 389–395, 2014, ISSN: 18766102. DOI: 10.1016/j.egypro.2014.08.111. [Online]. Available: http://dx.doi.org/10.1016/j.egypro.2014.08.111.

[56] C. Duran, "Bifacial Solar Cells : High Efficiency Design, Characterization, Modules and Applications," PhD thesis, University of Konstanz, 2012. DOI: 10.1093/nar/gng055.

[57] M. Schweiger and W. Herrmann, "Comparison of energy yield data of fifteen PV module technologies operating in four different climates," *IEEE 42nd Photovoltaics Specialists Conference (PVSC)*, pp. 1–6, 2015. DOI: 10.1109/PVSC.2015.7356123.

[58] G. S. Kinsey, "Spectrum sensitivity, energy yield, and revenue prediction of PV and CPV modules," *IEEE Journal of Photovoltaics*, vol. 5, no. 1, pp. 258–262, 2015, ISSN: 15517616. DOI: 10.1063/1.4931507.

[59] B. C. Duck and C. J. Fell, "Comparison of methods for estimating the impact of spectrum on PV output," in *IEEE 42nd Photovoltaics Specialists Conference (PVSC)*, IEEE, 2015, pp. 1–6, ISBN: 9781479979448. DOI: 10.1109/PVSC.2015.7356211.

[60] M. R. Lewis, E. M. Tonita, C. E. Valdivia, R.-J. K. Obhi, J. Leslie, M. I. Bertoni, and K. Hinzer, "Angular Dependence of Textured Bifacial Silicon Heterojunction Solar Cells for High Latitudes," in *IEEE 46th Photovoltaics Specialists Conference (PVSC)*, Chicago, IL, 2019, pp. 1919–1923, ISBN: 9781728104942. DOI: 10.1109/PVSC40753.2019.8980857.

[61] M. R. Lewis, A. C. J. Russell, C. E. Valdivia, J. E. Haysom, M. I. Bertoni, and K. Hinzer, "Impact of Air Mass on Energy Yield Calculation for Bifacial Silicon Heterojunction Photovoltaic Modules in High-Latitude Conditions," in *IEEE 47th Photovoltaic Specialists Conference (PVSC)*, Calgary, AB, 2020.

[62] A. Mecherikunnel and J. Richmond, "NASA Technical Memorandum 82021- Spectral Distribution of Solar Radiation," no. September 1980, p. 93, 1980.

[63] M. Lee and A. Panchula, "Spectral correction for photovoltaic module performance based on air mass and precipitable water," in *IEEE 43rd Photovoltaics Specialists Conference (PVSC)*, Portland, OR: IEEE, 2016, pp. 1351–1356, ISBN: 9781509027248. DOI: 10.1109/PVSC.2016.7749836.

[64] V. Tatsiankou, K. Hinzer, H. Schriemer, P. McVey-White, and R. Beal, "Deployment and early results from the CanSIM (Canadian Solar Spectral Irradiance Meter) network," *AIP Conference Proceedings*, vol. 1881, no. September, 2017, ISSN: 15517616. DOI: 10.1063/1.5001451.

[65] S. Nann and C. Riordan, "Solar Spectral Irradiance under Clear and Cloudy Skies: Measurements and a Semiempirical Model," *Journal of Applied Metrology*, vol. 30, pp. 447–462, 1991.

[66] D. L. King, W. E. Boyson, and J. A. Kratochvil, "Analysis of factors influencing the annual energy production of photovoltaic systems," in *IEEE 29th Photovoltaic Specialists Conference (PVSC)*, New Orleans, LA, USA, 2002, pp. 1356–1361, ISBN: 0780374711. DOI: 10.1109/pvsc.2002.1190861.